

Three-dimensional Integrated Functional, Structural, and Computational Mapping to Define the Structural “Fingerprints” of Heart-Specific Atrial Fibrillation Drivers in Human Heart Ex Vivo

Jichao Zhao, PhD; Brian J. Hansen, BSc; Yufeng Wang, BT; Thomas A. Csepe, BSc; Lidiya V. Sul, BSc; Alan Tang, BSc; Yiming Yuan, BSc; Ning Li, MD, PhD; Anna Bratasz, PhD; Kimerly A. Powell, PhD; Ahmet Kilic, MD; Peter J. Mohler, PhD; Paul M. L. Janssen, PhD; Raul Weiss, MD; Orlando P. Simonetti, PhD; John D. Hummel, MD; Vadim V. Fedorov, PhD

Background—Structural remodeling of human atria plays a key role in sustaining atrial fibrillation (AF), but insufficient quantitative analysis of human atrial structure impedes the treatment of AF. We aimed to develop a novel 3-dimensional (3D) structural and computational simulation analysis tool that could reveal the structural contributors to human reentrant AF drivers.

Methods and Results—High-resolution panoramic epicardial optical mapping of the coronary-perfused explanted intact human atria (63-year-old woman, chronic hypertension, heart weight 608 g) was conducted during sinus rhythm and sustained AF maintained by spatially stable reentrant AF drivers in the left and right atrium. The whole atria ($107 \times 61 \times 85 \text{ mm}^3$) were then imaged with contrast-enhancement MRI (9.4 T, $180 \times 180 \times 360\text{-}\mu\text{m}^3$ resolution). The entire 3D human atria were analyzed for wall thickness (0.4–11.7 mm), myofiber orientations, and transmural fibrosis (36.9% subendocardium; 14.2% midwall; 3.4% subepicardium). The 3D computational analysis revealed that a specific combination of wall thickness and fibrosis ranges were primarily present in the optically defined AF driver regions versus nondriver tissue. Finally, a 3D human heart-specific atrial computer model was developed by integrating 3D structural and functional mapping data to test AF induction, maintenance, and ablation strategies. This 3D model reproduced the optically defined reentrant AF drivers, which were uninducible when fibrosis and myofiber anisotropy were removed from the model.

Conclusions—Our novel 3D computational high-resolution framework may be used to quantitatively analyze structural substrates, such as wall thickness, myofiber orientation, and fibrosis, underlying localized AF drivers, and aid the development of new patient-specific treatments. (*J Am Heart Assoc.* 2017;6:e005922. DOI: 10.1161/JAHA.117.005922.)

Key Words: 3D computer model • atrial fibrillation • atrial structure • computer-based model • fiber architecture • fibrosis • human atria • reentry • wall thickness

Atrial fibrillation (AF) is the most common sustained heart rhythm disturbance.¹ Current ablation strategies for persistent/permanent AF or AF with concurrent cardiac diseases are disappointing, with a <30% long-term success rate for single-ablation procedures.^{1–3} This inadequate success rate may be because of the lack of basic understanding of the underlying atrial functional and structural substrates that sustain AF directly in human hearts^{4–7} and emphasizes

the need for quantitative tools to evaluate human atrial 3-dimensional (3D) structural features in both clinical and experimental settings.

It has been suggested that AF may be driven by discrete reentrant drivers,^{6–8} ablation of which could treat the arrhythmia. However, current clinical structural imaging, including late gadolinium-enhanced MRI⁹, and electrode mapping approaches, lack the necessary resolution to resolve

From the Auckland Bioengineering Institute, The University of Auckland, New Zealand (J.Z., Y.W., A.T., Y.Y.); Departments of Physiology & Cell Biology (B.J.H., T.A.C., L.V.S., N.L., P.M.L.J., V.V.F.), Surgery (A.K.), Internal Medicine (P.J.M., R.W., J.D.H.), and Biomedical Informatics (O.P.S.) and Davis Heart & Lung Research Institute (B.J.H., T.A.C., N.L., A.B., K.A.P., A.K., P.J.M., P.M.L.J., R.W., O.P.S., J.D.H., V.V.F.), The Ohio State University Wexner Medical Center, Columbus, OH.

Accompanying Data S1 and Figures S1 through S3 are available at <http://jaha.ahajournals.org/content/6/8/e005922/DC1/embed/inline-supplementary-material-1.pdf>

Correspondence to: Vadim V. Fedorov, PhD, Department of Physiology and Cell Biology, The Ohio State University Wexner Medical Center, 300 Hamilton Hall, 1645 Neil Ave, Columbus, OH 43210-1218. E-mail: vadim.fedorov@osumc.edu

Received May 4, 2017; accepted June 29, 2017.

© 2017 The Authors. Published on behalf of the American Heart Association, Inc., by Wiley. This is an open access article under the terms of the Creative Commons Attribution-NonCommercial-NoDerivs License, which permits use and distribution in any medium, provided the original work is properly cited, the use is non-commercial and no modifications or adaptations are made.

Clinical Perspective

What Is New?

- The novel 3-dimensional structural analysis based on histologically validated contrast-enhanced MRI reports for the first time collective quantification of the entire human 3-dimensional atrial architecture, including atrial wall thickness variation, transmural fibrosis distribution, and myofiber orientation, with 180- μm resolution.
- Through integration of high-resolution optical mapping with contrast-enhanced MRI, this study provides the first direct evidence that atrial fibrillation reentrant drivers may be identifiable by their distinct structural “fingerprints,” which consist of a specific combination of intermediate wall thickness, intermediate fibrosis, and twisted myofiber orientation.

What Are the Clinical Implications?

- Our novel 3-dimensional computational framework can be applied to clinical delayed-enhancement MRI to quantitatively analyze the structural reentrant atrial fibrillation driver “fingerprints” and may provide a novel method for predicting atrial fibrillation driver locations and improving patient-specific ablation therapies.
- This study suggests that 3-dimensional computational analysis of integrated electrophysiological and structural mapping may eventually shift the ablation paradigms from extensive ablation of poorly estimated targets to a new mechanism-based, minimally damaging, targeted treatment of patient-specific “fingerprints” harboring reentrant atrial fibrillation drivers.

the defining structural–functional characteristics or “fingerprints” of AF drivers, including but not limited to transmural arrhythmogenic fibrosis, wall thickness variations, and myofiber misalignment.^{6–8} To date, there are no tools available to systematically analyze important structural characteristics, such as fibrosis distribution patterns, myofiber orientations, and wall thickness, across both atrial chambers in the human heart because of the inherent complexity of the atrial wall and the low resolution of current clinical imaging technology.^{10–14}

Large-animal structural models, such as sheep^{15,16} and goats,¹⁷ have been used to investigate myofiber structure and surface geometry of the intact atria and progress has been made in defining the mechanisms of AF in animal models.^{4,18} However, the interspecies difference in atrial structure and physiology may diminish the translational applications of these models to human AF.⁷ The first realistic human atrial structural model was developed from cryosection images with a spatial resolution of 330 μm^3 of a deceased 59-year-old woman, but the model only included fiber orientations that

were limited to major muscular bundles and lacked information on fibrosis.¹⁰ The explanted human atrial myofiber structure was recently studied using a micro-computed tomographic imaging with 49- μm^3 resolution integrated with functional optical mapping data to investigate the effect of atrial structure on sinus rhythm and arrhythmia activation patterns.¹⁹ Furthermore, myofiber orientations of ex vivo human atria were also studied by diffusion tensor approach²⁰ using clinical 3 T MRI with $\approx 400\text{-}\mu\text{m}^3$ resolution. However, these methodologies cannot visualize fibrosis, which may play a crucial role in AF maintenance mechanisms and specifically in AF driver location and spatial stability.^{9,21,22}

To overcome these limitations, our group recently developed an integrated approach in which fibrosis detection by high-resolution (up to 80 μm^3) 3D contrast-enhanced MRI (CE-MRI) was validated in the human heart by histological studies,⁸ and clinical relevance was shown through a proof-of-concept in vivo study.²³ CE-MRI of functionally mapped atria can be used to analyze the influence of atrial structure on AF driver track formation and arrhythmia maintenance. In our recent ex vivo human study, we have demonstrated that human AF may be driven by microanatomic reentrant AF drivers anchored to fibrotically insulated tracks within the complex atrial wall. Moreover, the study highlighted the essential role of transmural fibrosis, myofiber orientation, and wall thickness in sustaining AF in the human lateral right atria (LRA).⁸ The study suggests that if structural fingerprints unique to AF driver regions can be found, then structural analysis of the entire atria could predict AF driver locations with assigned probabilities.

In the present study, we have developed novel detailed structural analysis of 3D CE-MRI of the explanted intact human atria, which provides the first systematic computational analysis of intact and entire 3D human atrial structure (wall thickness, histologically validated transmural fibrosis, and 3D myofiber orientation). In addition, we utilized 3D computer simulations based on structural and functional imaging data of the same intact human atria with unprecedented highest spatial resolution to study the mechanisms sustaining AF.

Methods

An expanded Methods section can be found in Data S1.

Ex Vivo Intact Human Atria and Bi-Atrial Optical Mapping

An intact explanted human heart¹⁹ (Heart #947200, motor vehicle accident, rejected for transplant because of age and comorbidities, 63-year-old woman, chronic hypertension, hypothyroidism, previous hysterectomy, heart weight 608 g) from the Lifeline of Ohio Organ Procurement Organization was

obtained in the operating room at the time of cross-clamp in accordance with The Ohio State University Institutional Review Board. The Institutional Review Board waived requirements for consent. Whole intact atria were dissected from ventricles and coronary-perfused with oxygenated Tyrode solution. Subepicardial, bi-atrial optical mapping with near-infrared voltage-sensitive dye di-4-ANBDQBS was conducted during sinus rhythm, posterior left atrium (PLA) pacing, and burst pacing-induced sustained AF. The activation maps were recently published in Zhao et al¹⁹ for this heart. Throughout the experiments, a high spatial (100×100 pixels) and temporal (1 ms) resolution UltimaL CMOS camera (SciMedia, Japan) was focused on both atrial chambers (116×116 mm² optical field of view) to achieve maximal coverage of the atria. AF drivers were defined as sustained rotational activity in the area of highest dominant frequency.⁸

Ex Vivo CE-MRI of Human Atria

After the functional mapping experiment, the human atria were formalin fixed and kept at 4°C. To prepare the heart for CE-MRI, it was washed out with phosphate buffered saline and then incubated at 4°C in 0.2% Gd-DTPA (dimeglumine gadopentetate Magnevist; Bayer Schering Pharma) for 7 days as previously described for human LRA.⁸ CE-MRI was performed using a 9.4 T Bruker BioSpin Spectrometer (Ettlingen, Germany) and a 72-mm volume coil at a resolution of 180×180×360 μm³. CE-MRI images of the human atria (107×61×85 mm³) were interpolated to an isotropic resolution of 180 μm³, segmented, and smoothed using a custom Matlab program (MathWorks) and visualized in 3D using Amira (FEI Company) (Figure 1 and Figure S1).^{23,24} Optical maps and the reconstructed 3D human atrial model were reconciled using atrial anatomical landmarks.⁸

3D Bi-Atrial Wall Thickness

In this study, a robust approach to estimate the 3D atrial wall thickness across both atrial chambers was used to solve the Laplace equation with 2 different boundary conditions specified at both epicardial and endocardial surfaces from reconstructed CE-MRI and then tracing trajectories/distances between the 2 surfaces along the local gradient of the resultant Laplace solutions (Figure S2).^{25,26} The Laplace solutions were also used to divide the 3D atrial tissue into 3 equal size subvolumes: subendocardium, midwall, and subepicardium (Figure 2).

3D Fibrosis Estimation

Image voxels containing fibrotic tissue have a higher signal intensity compared with nonfibrotic voxels when imaged using CE-MRI.^{8,24} Fibrosis was measured from CE-MRI images by

applying a global fibrosis mask color coded to show transmural (Figure 3A). Fibrosis quantification was validated by using a least-square approximation based on a sequence of local fibrosis threshold values from 2D CE-MRI images (resliced and interpolated by using Amira) and matched Masson's trichrome staining with 0.5-μm² resolution (Figure 3C).⁸ Fibrosis density was constructed for each voxel by determining the percent of neighboring fibrotic voxels within a radius of 5 pixels (Figures 4 and 5).

3D Myofiber Estimation

The structure tensor approach utilized the signal intensity variation of the CE-MRI images and 3D Eigen-analysis to estimate 3D fiber orientations by modeling local fiber alignment as the orientation with the least signal variation (Figures 6 and 7), as described in detail in our previous work.^{15,19,24}

Modeling 3D Atrial Electrical Propagations

The spread of electrical activation in the realistic 3D human atrial geometry can be simulated by solving the cardiac monodomain equation using a voxel-based finite difference solver.^{10,27} In this study, we have adapted the simplified 3-current Fenton-Karma cellular activation models to recreate the optically recorded regional conduction velocities and action potential durations (APDs) in the PLA region from the same heart, which was then applied across both atria of the model (Figure 8).^{15,28} Atrial 3D geometry with a resolution of 180 μm³ including accurate wall thickness, myofiber orientations, and transmural fibrosis, was integrated with the adapted cellular model into a 3D computer model. Electrical conductivities were set at an anisotropic ratio of 9:1, which led to ≈3:1 regional anisotropic ratio for conduction velocities along the long axis of the cell and allowed the proper reproduction of the experimentally mapped conduction velocities as utilized by previous atrial modeling studies.^{4,15} Fibrosis and simulated ablation lesion lines were modeled as nonconducting tissue.^{4,29} The simulated activation time maps were interpolated, smoothed, and visualized on the epicardial surface mesh of the human atria. A total of 12 atrial locations were chosen in computer models as pacing sites for trains of stimuli with gradually reduced coupling intervals until either arrhythmia was induced or conduction failed (Figure 8G through 8I). Computer simulations of reentrant drivers were run for 10 s before either intervention or conclusion of the simulation.

Statistical Analysis

Differences between driver and nondriver regions were estimated using the nonparametric Mann–Whitney test in

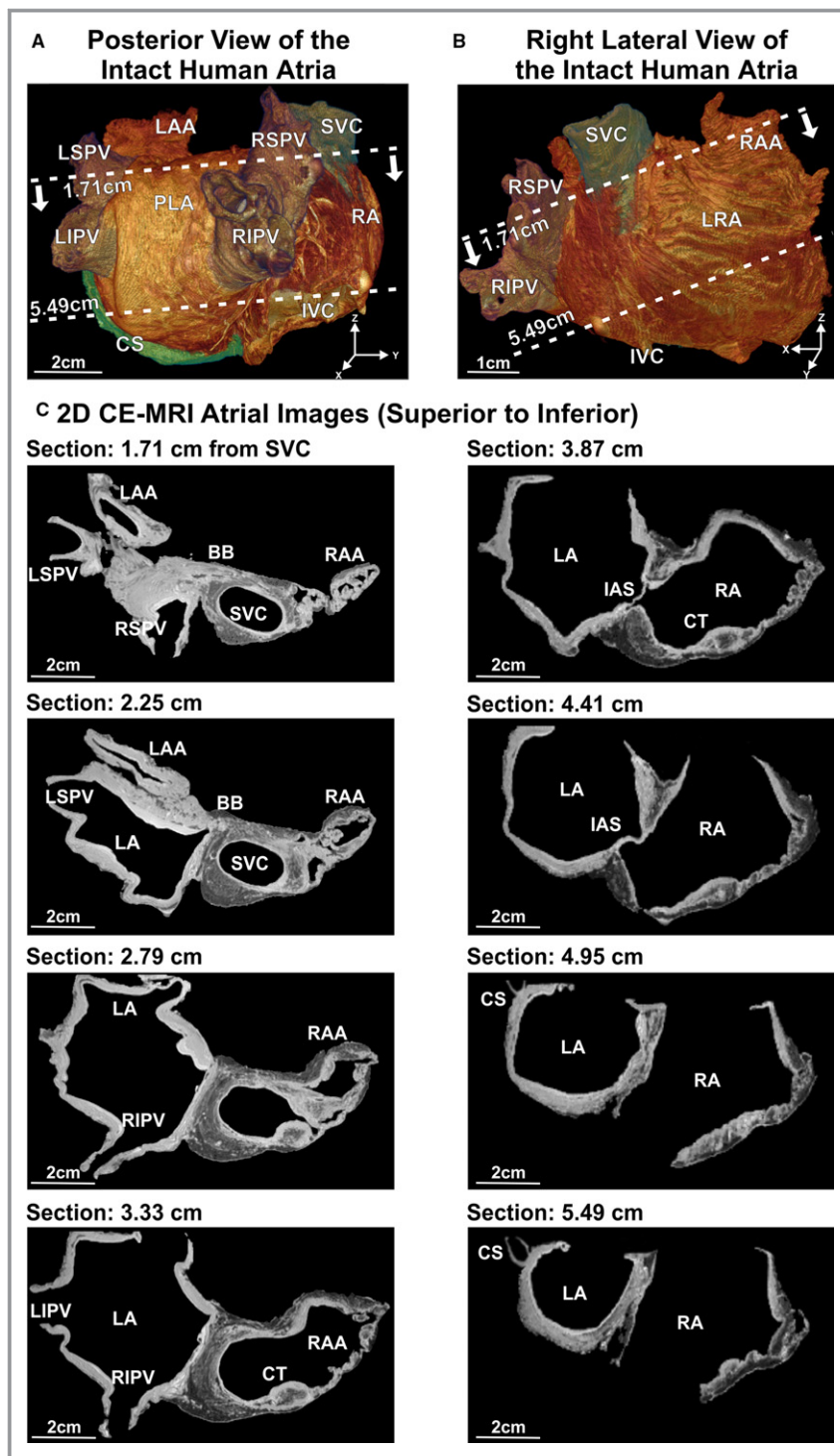


Figure 1. Intact human atria imaged using CE-MRI. The explanted intact human atria were visualized in 3-dimensional (3D) from a posterior (A) and right lateral (B) view. CS is highlighted in green in (A). C, Typical 2-dimensional (2D) raw CE-MRI images are displayed from the top to the bottom of the 3D atrial volume with a spatial distance of 0.54 cm from the SVC, and their locations from the SVC are indicated by the dashed lines in (A and B). BB indicates Bachmann’s bundle; CE-MRI, contrast-enhanced magnetic resonance imaging; CS, coronary sinus; CT, crista terminalis; IAS, interatrial septum; IVC/SVC, inferior/superior vena cava; LA/RA, left/right atrium; LAA/RAA, left/right atrial appendage; LRA, lateral right atrium; LSPV/LIPV/RSPV/RIPV, left superior/left inferior/right superior/right inferior pulmonary vein; PLA, posterior left atrium.

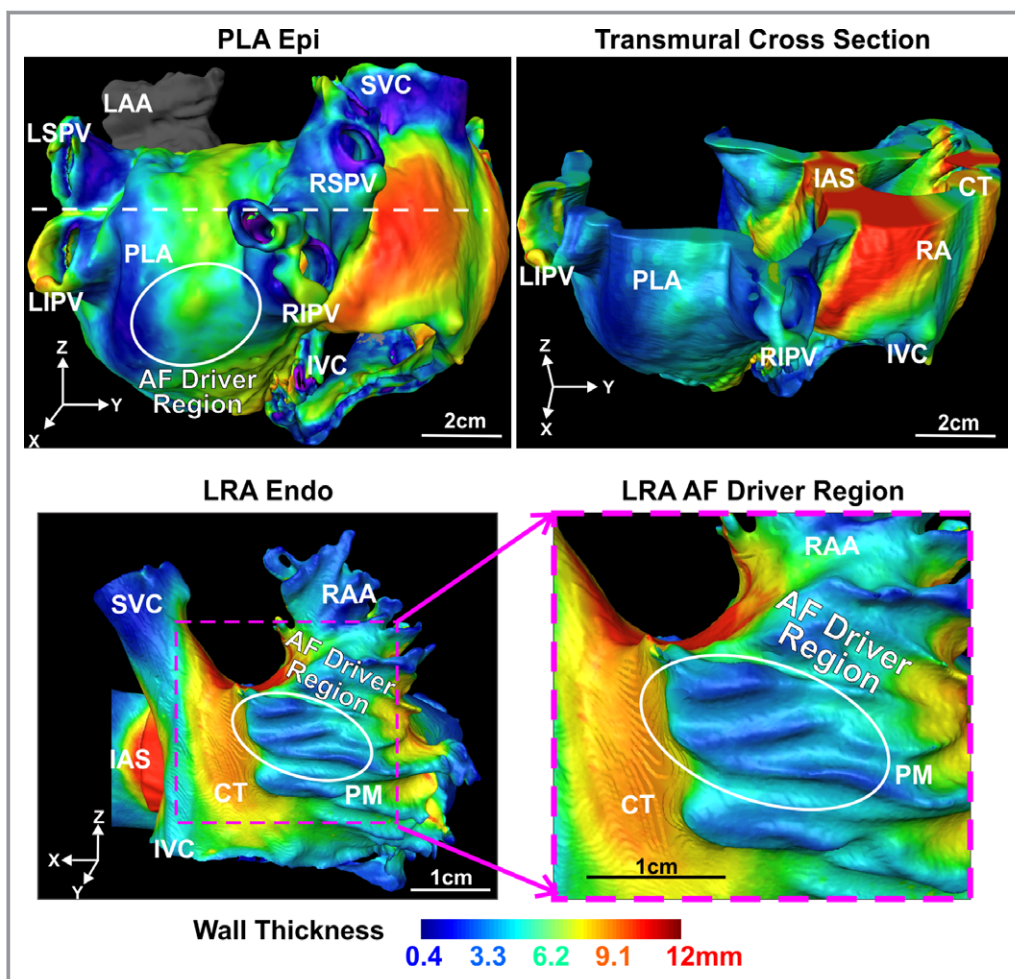


Figure 2. Three-dimensional (3D) atrial wall thickness variation across the whole human atria. Top left, 3D bi-atrial wall thickness of the human atria is superimposed on the atrial epicardium and displayed from the posterior view. Top right, transmural cross section of human atria. Bottom left, 3D wall thickness of the LRA is superimposed on the atrial endocardium and displayed from the right lateral view. Bottom right, enhanced view of the AF driver region in the LRA. The white ovals indicate the locations of AF driver regions defined by optical mapping. AF indicates atrial fibrillation; CT, crista terminalis; Endo, endocardium; Epi, epicardium; IAS, interatrial septum; IVC/SVC, inferior/superior vena cava; RA, right atrium; LAA/RAA, left/right atrial appendage; LRA, lateral right atrium; LSPV/LIPV/RSPV/RIPV, left superior/left inferior/right superior/right inferior pulmonary vein; PLA, posterior left atrium; PMs, pectinate muscles.

Minitab 17. Data are presented as mean±SD or median and 95% confidence interval.

Results

Structural Characteristics of the Intact Human Atria

The intact human heart contained all key atrial regions,³⁰ such as coronary sinus, crista terminalis, Bachmann’s bundle, pulmonary veins (PVs), left/right atrial appendage, PLA, and pectinate muscles. The 3D segmented human atria with 180- μm^3 resolution are displayed at a posterior view (Figure 1A)

and right lateral view (Figure 1B). Eight typical 2D CE-MRI images are shown in Figure 1C. Cavity volumes of left (LA) and right atrium (RA) were 41.4 and 47.4 cm^3 , respectively.

The estimated 3D atrial wall thickness maps demonstrated that the atrial septum, LRA, and anterior LA were the thickest regions, and the PVs and superior/inferior vena cava were the thinnest (Figure 2). The mean wall thickness for LA versus RA was 3.7 ± 1.7 mm versus 4.2 ± 2.3 mm (Table). Furthermore, RA had a wider range from 0.4 to 11.7 mm, compared with LA from 1.1 to 8.6 mm. Thicker areas of the atria bordered thinner regions in the PLA, LA roof and floor, and a complex thickness variation pattern was observed in the LRA (Figure 2).

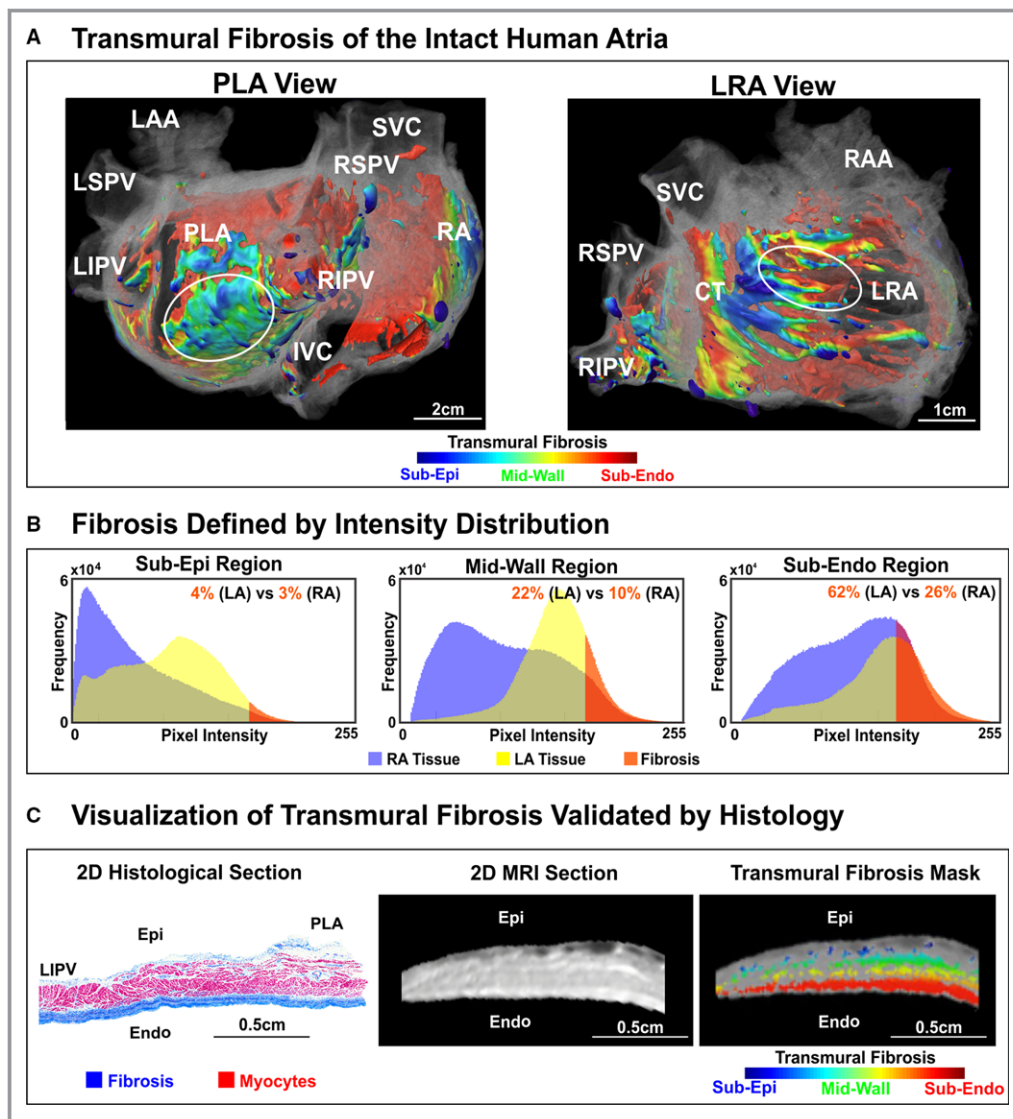


Figure 3. Three-dimensional (3D) fibrosis distribution across the whole human atria. A, 3D fibrosis distribution in atrial volume was color-coded and visualized transmurally using a rainbow color spectrum: blue for epicardium and red for endocardium. Fibrosis transmuralities are displayed in the PLA and LRA, respectively. The white ovals indicate the locations of AF driver regions defined by optical mapping. B, The original color intensity distribution of the CE-MRI images is plotted in subepicardium (epi), midwall, and subendocardium (endo) regions. Here blue, yellow, and orange are used to show the number of voxels of the RA, LA, and identified fibrosis, respectively. C, The fibrosis threshold value was chosen by matching 2-dimensional (2D) histology sections stained by Masson's trichrome (left) to 2D CE-MRI images (middle); then a color mask was applied to show transmural fibrosis (right). AF indicates atrial fibrillation; CE-MRI, contrast-enhanced magnetic resonance imaging; CT, crista terminalis; Endo, endocardium; Epi, epicardium; IAS, interatrial septum; IVC/SVC, inferior/superior vena cava; LA/RA, left/right atrium; LAA/RAA, left/right atrial appendage; LRA, lateral right atrium; LSPV/LIPV/RSPV/RIPV, left superior/left inferior/right superior/right inferior pulmonary vein; PLA, posterior left atrium.

Original CE-MRI images had adequate signal intensity contrast between atrial myocardium and fibrotic tissue (Figures 1C and 3C) so that fibrosis could be identified and analyzed. Transmurial fibrosis was heterogeneously distributed through the varying thickness of the 3D atrial wall. Fibrosis occupied 36.9% of the subendocardium, 14.2% of the midwall,

and 3.4% of the subepicardium of the whole human atria (Figure 3A and 3B, Table). Subepicardial fibrosis was mainly clustered in the inferior PLA and LRA. The LA subendocardium contained 61.9% fibrotic tissue concentrated in the PLA, LA roof, and floor, while the RA subendocardium contained only 25.7% fibrotic tissue, mainly in the LRA (Figure 3A). Our CE-

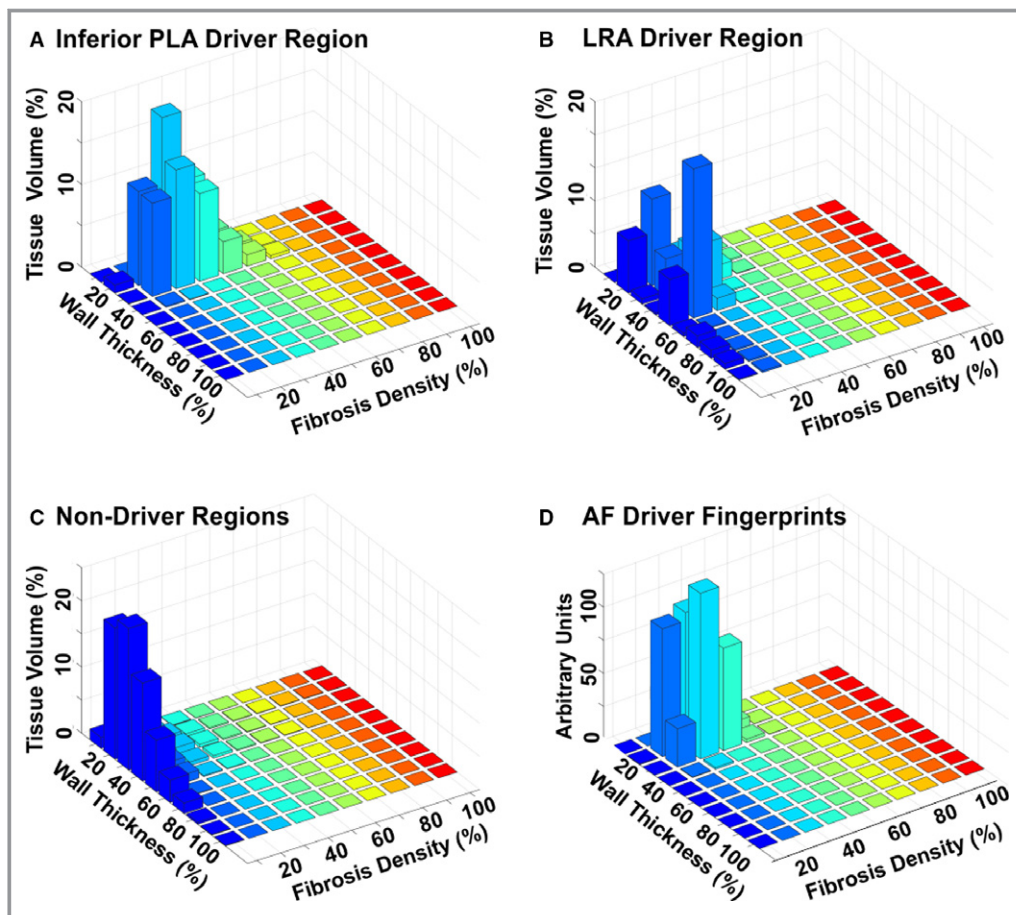


Figure 4. Optical mapping defined AF driver regions have structural characteristics distinct from nondriver regions. The proportion (%) of the atrial volume for varying combinations of normalized wall thickness and fibrosis density is shown for the PLA driver region (A), LRA driver region (B), and nondriver regions (C). D, AF driver fingerprints, defined by fibrosis density and wall thickness ranges by weighting positively with driver regions and negatively with nondriver regions, were found to be most specific at normalized wall thickness (20–30%) and fibrosis density (20–30%). Wall thickness was normalized to the minimum and maximum values (0%=0.4 mm, 100%=11.7 mm). AF indicates atrial fibrillation; LRA, lateral right atrium; PLA, posterior left atrium.

MRI and other studies³⁰ indicate a thin endocardial layer (0.1–0.7 mm) of predominantly fibrous tissue in the left atria, which explains why the highest percent of fibrosis was observed in the LA endocardium. The functional effect of this endocardial layer of fibrous tissue needs to be evaluated in future studies.

Analysis of CE-MRI images accurately estimated 3D myofiber orientations, which are displayed and color-coded relative to an inclination angle shown in Figure 6. The fiber pattern in the LA was characterized by general circumferential orientations in the atrial roof and floor, and vertical tracts in the PLA. The atrial roof and LRA regions were dominated by major muscular bundles, the extension of Bachmann’s bundle, crista terminalis, and pectinate muscles, where myofibers were organized and oriented along the long axis of the bundles. Other areas throughout the

human atria were characterized by more disorganized fiber orientations.^{15,30}

3D Atrial Structural Fingerprints of AF Driver Regions

Bi-atrial optical mapping revealed stable and long-lasting reentrant AF drivers.¹⁹ Several reproducible, pacing-induced episodes of AF were sustained by 2 reentrant AF drivers in the superior and inferior PLA regions with frequencies of 7.6 Hz up to 70 minutes. Fibrillatory activity in 1 AF episode with 2 PLA drivers spontaneously converted to activity with a single reentrant driver in the LRA with a frequency of 4.5 Hz for 49 s. The inferior PLA reentrant driver was spatially stable within a 24×33 mm² region at the junction of the right inferior PV with the atrial floor. The AF driver

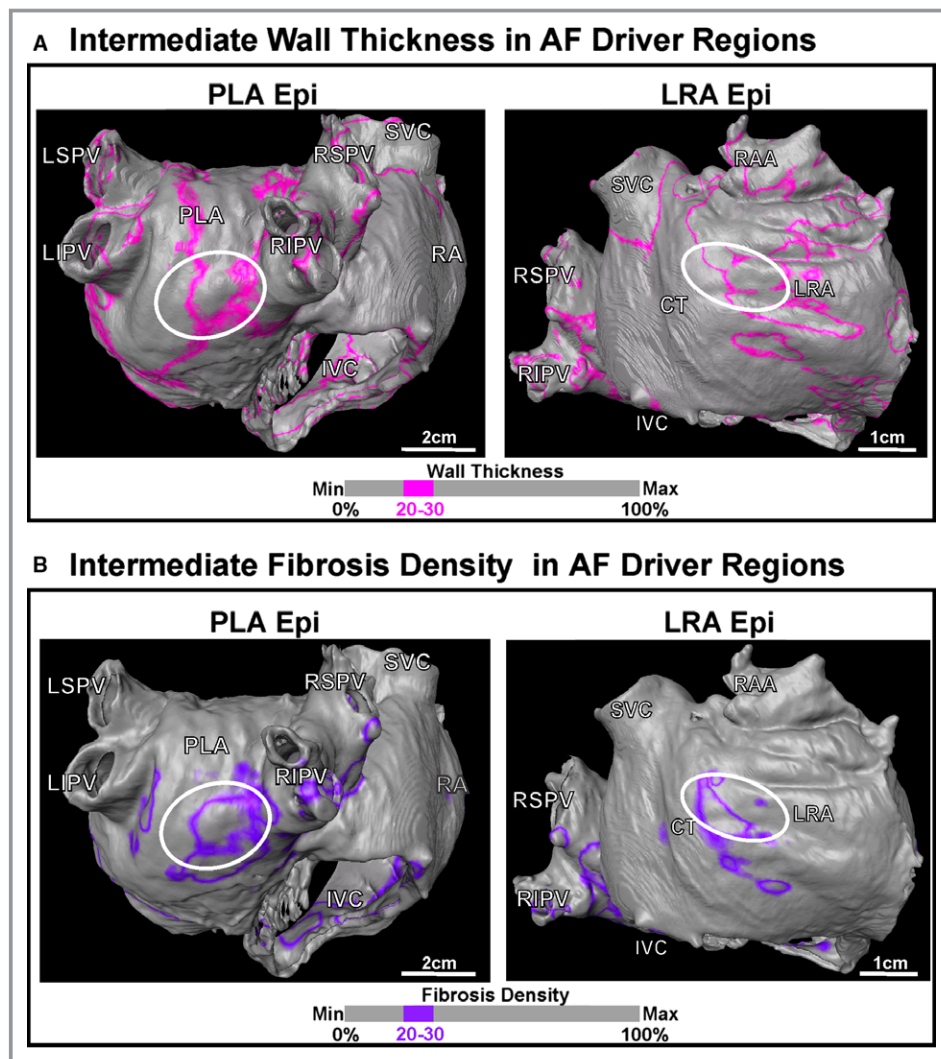


Figure 5. Three-dimensional dispersion of intermediate wall thickness and fibrosis across the whole human atria. A, Intermediate wall thickness regions (pink) of the human atria are displayed from the PLA and LRA views. B, Intermediate fibrosis regions (purple) of the human atria displayed from the PLA and LRA views. C, Regions of both intermediate wall thickness and fibrosis (orange) act as fingerprints by distinguishing AF driver regions from the whole atria. The white ovals indicate the locations of AF driver regions defined by optical mapping. AF indicates atrial fibrillation; CT, crista terminalis; Epi, epicardium; IVC/SVC, inferior/superior vena cava; RA, right atrium; RAA, right atrial appendage; LRA, lateral right atrium; LSPV/LIPV/RSPV/RIPV, left superior/left inferior/right superior/right inferior pulmonary vein; PLA, posterior left atrium.

region was characterized by wall thickness varying between thicker green) and thinner (blue) tissue (Figure 2), and clusters of transmural fibrosis (left panel of Figure 3A). The superior PLA driver was excluded from initial quantitative analysis of driver fingerprints in this study because its exact driver track was hidden from optical mapping by the curvature of the atrial roof. The LRA driver was located within a region $10 \times 19 \text{ mm}^2$ of the pectinate muscle complex with highly variable thickness (Figure 2) and fibrosis strands (Figure 3B).

The specific range of fibrosis and wall thickness that distinguished driver regions from nondriver regions was determined quantitatively by weighing the full ranges positively with the ranges found in the inferior PLA and LRA driver regions (Figure 4A and 4B) and inversely with nondriver regions (Figure 4C). This analysis found that driver regions were characterized by a higher proportion of wall thickness that was 20% to 30% of the total thickness range and a higher proportion of tissue with 20% to 30% fibrosis density (Figure 4D). The wall thickness range (20–30%) prevalent in

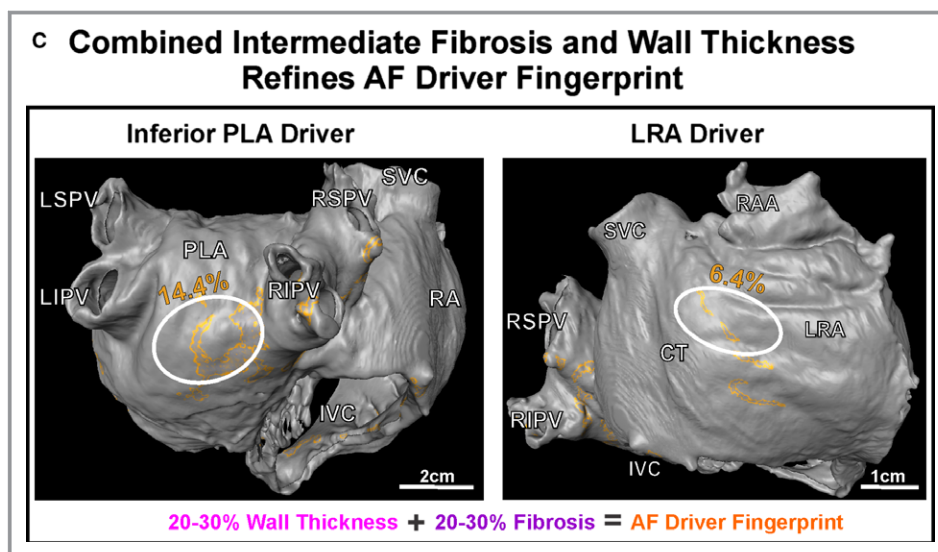


Figure 5. Continued.

the driver regions, defined as intermediate wall thickness, was highlighted across the whole atria as shown in Figure 5A. Similarly, the fibrosis density range (20–30%) prevalent in driver regions, defined as intermediate fibrosis, was also highlighted across the whole atria (Figure 5B). More importantly, highlighting only regions that fell within the intermediate ranges for both fibrosis density and wall thickness (Figure 5C) revealed some of the structural characteristics that may define AF driver fingerprints. These fingerprints covered 14.4% of the inferior PLA driver region and 6.4% of the LRA driver region.

Additionally, we discovered that the 2 AF drivers were located in atrial tissue with sharp myofiber twists. The inferior PLA reentrant driver was located at the intersection of the circumferential atrial floor myofibers and vertical PLA myofibers (Figure 6A). Furthermore, part of the LRA reentrant circuit was situated at the intersections between the vertical crista terminalis and horizontal pectinate muscles (Figure 6B). Interestingly, fibrosis clustered in strands along myofiber orientations that may further enhance the structural anisotropy and represent additional components of AF driver fingerprints (Figure 6).

Next, we attempted to use the results from the structural analysis to define the proportion of fingerprints in the superior PLA driver region. The fingerprints optimized using the parameters of the inferior PLA and LRA driver regions were able to identify 6.7% of fingerprints in this superior PLA driver region ($\approx 18 \times 25 \text{ mm}^2$) suggested by optical mapping¹⁹ (Figure 7). Furthermore, to robustly test that randomly resampling the remaining human atrial tissue with similar size (9-mm-radius spheres) to the 3 driver regions consistently shows a lower proportion of fingerprints, we have sequentially, randomly generated 99 such regions within nondriver regions (MathWorks,

Inc.). The median proportion of fingerprints for nondriver regions is 0.03% (95% confidence interval, 0.01–0.117%) and mean $0.42 \pm 0.99\%$, which is significantly lower than the median of the 3 driver regions 6.7% (95% confidence interval, 6.4–14.4%) and mean $9.17 \pm 4.53\%$ ($P < 0.0029$).

Functionally and Structurally Realistic Human Atria 3D Computer Model

We sought to develop an integrated computational AF model based on high-resolution functional mapping (APDs and conduction velocities) (Figure 8A through 8C) and structural mapping (atrial geometry, fibrosis, and myofiber orientations) (Figures 2, 3, and 6). The detailed 3D human atria computer model was developed to reproduce optically recorded electrical activation patterns during sinus rhythm (Figure 8D) and PLA pacing (Figure 8E), as well as the APD distribution during PLA pacing (Figure 8F). The computer model was then used to investigate the contribution of structure to AF. Reentrant drivers were induced from 4 of 12 stimulation sites (Figure 8G), either in the inferior/superior PLA or LRA regions. For illustration, simulated reentry in the inferior PLA induced by pacing from the atrial floor or from the right inferior PV is displayed in Figure 8H and 8I, and Figure 9A. On the other hand, computer models lacking myofiber orientations and fibrosis data failed to induce sustained AF from any of the 12 pacing locations (Figure 9C).

3D Computer Model to Evaluate Different Ablation Approaches

We then evaluated the computer model's efficiency for testing different ablation procedures on the same AF drivers

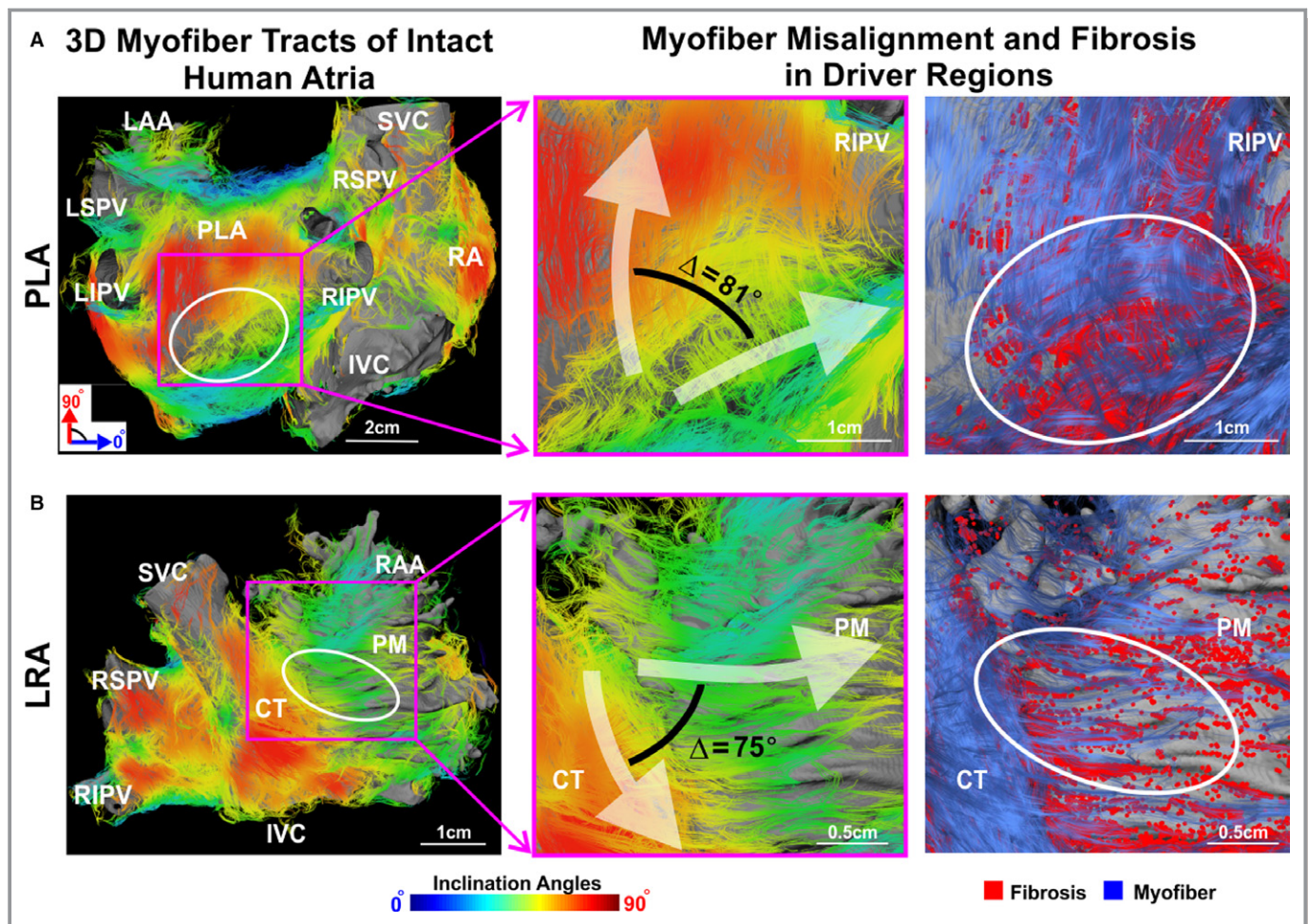


Figure 6. Three-dimensional (3D) myofiber tracts of the intact human atria show misalignment in AF driver regions. 3D myofiber tracts colored by absolute inclination angles between 0° to 90° are displayed from the PLA (A) and LRA (B) views. Here blue is coded for circumferential angles and red for verticals with reference to the imaging coordinates. Right: Fibrosis tends to deposit along the myofiber orientations to enhance structural and electrical anisotropy. AF indicates atrial fibrillation; CT, crista terminalis; IVC/SVC, inferior/superior vena cava; RA, right atrium; LAA/RAA, left/right atrial appendage; LRA, lateral right atrium; LSPV/LIPV/RSPV/RIPV, left superior/left inferior/right superior/right inferior pulmonary vein; PLA, posterior left atrium; PMs, pectinate muscles.

in the same atrial structure to design optimal heart-specific ablation procedures. The 3D mask mimicking transmural ablation lesions (diameter ≈ 5 mm) was treated as unexcitable regions in the computer model. We tested the ablation strategy that disrupts the microanatomic track of the reentrant driver with a single linear ablation lesion drawn from the reentrant driver to the nearest anatomical border as developed in Hansen et al.⁸ Targeted ablation ($\approx 2\text{-cm}^2$ area) forming a line from the center of the inferior PLA reentrant track to the right inferior PV terminated the reentry effectively and prevented the reinduction of arrhythmia (Figure 9B). Simulated PV isolation had almost no impact on the AF driver and failed to terminate AF (Figure S3A). A driver regional ablation approach that targeted the area of rotation with an area $\approx 3.1\text{ cm}^2$ slowed

AF (Figure S3B) and only terminated AF if increased to $>4\text{ cm}^2$.

Discussion

To the best of our knowledge, this is the first systematic analysis performed on structurally and functionally imaged intact human atria. The novel structural analysis in this study illustrates the complex wall thickness variation, transmural fibrosis distribution, and 3D myofiber architecture of the human heart. Moreover, AF reentrant drivers in this heart were distinguishable by fingerprints of specific intermediate wall thickness and fibrosis combined with twisted myofiber orientation. The subsequent computer model allowed us to investigate inducibility and maintenance of AF drivers in the

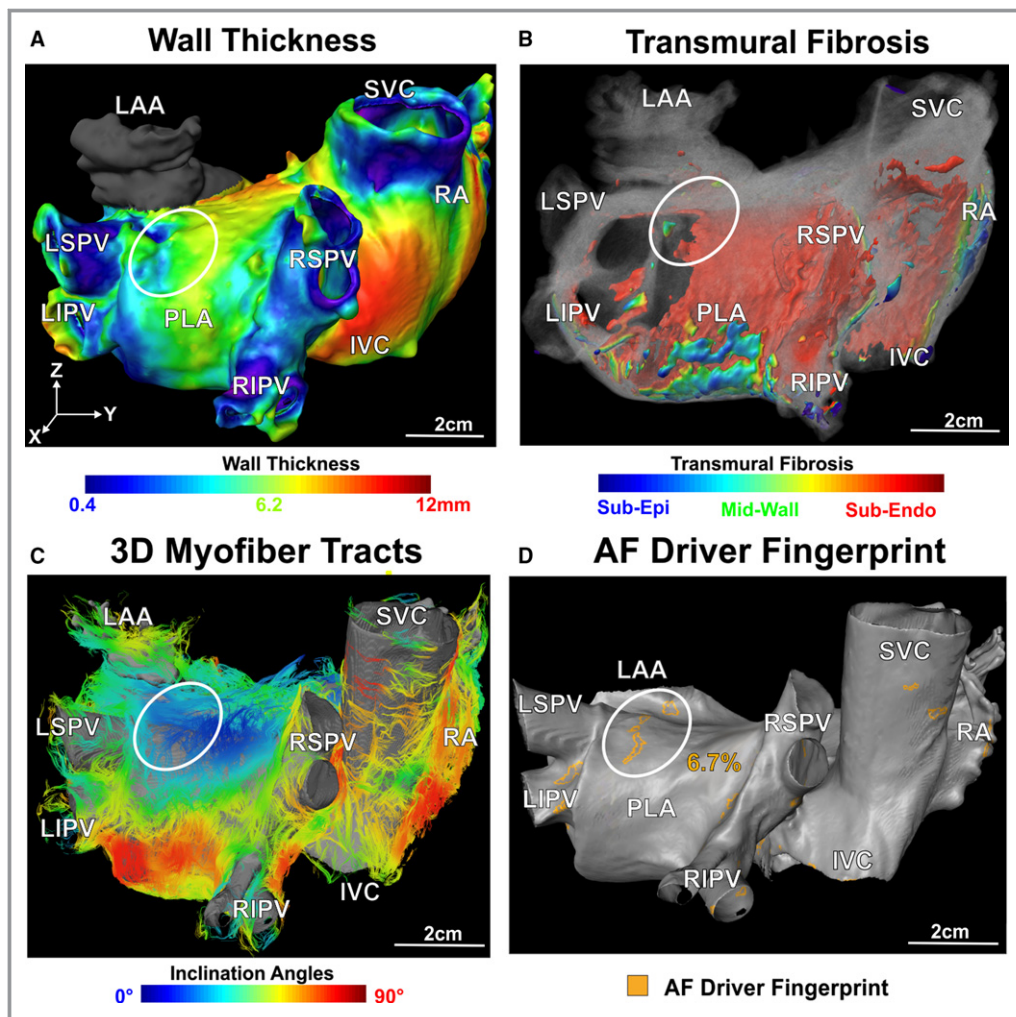


Figure 7. Structural fingerprints in the superior PLA driver region. A, Three-dimensional (3D) bi-atrial wall thickness of the human atria is superimposed on the atrial epicardium and displayed at the posterior roof view. B, 3D fibrosis distribution in atrial volume was color-coded and visualized transmurally using a rainbow color spectrum as in Figure 3A. C, 3D myofiber tracts visualized in the superior PLA driver region. D, Driver structural fingerprints dispersion in the superior PLA driver region (endocardial view) based on Figure 5C. The white ovals indicate the location of the superior PLA driver region suggested by optical mapping. AF indicates atrial fibrillation; IVC/SVC, inferior/superior vena cava; RA, right atrium; LAA/RAA, left/right atrial appendage; LSPV/LIPV/RSPV/RIPV, left superior/left inferior/right superior/right inferior pulmonary vein; PLA, posterior left atrium.

presence and absence of detailed underlying atrial structure, therefore providing insight about the crucial role of underlying structural contributors in sustaining AF.

Role of Atrial Structure in Sustaining AF

Since the early 20th century when Lewis et al³¹ proposed that a single reentry could sustain and drive AF, many explanations have been suggested for the mechanisms driving AF as we have recently reviewed.⁷ However, most studies accept the importance of atrial structure, and all mechanisms would benefit from a method that can quantify the

contribution of atrial structural substrates to AF maintenance.^{32–39} Spach and colleagues were the first to report local conduction delay and morphological changes in electrical signals caused by abrupt changes in myofiber orientations and geometric tissue variations in the dog atria *ex vivo*.⁴⁰ They subsequently presented the concept of nonuniform anisotropic reentry, where myofiber orientations and collagen act as substrates for microanatomic reentry in diseased human atria.⁴¹ Atrial wall thickness variation may influence AF activation patterns²⁵; particularly, tissue thickness variation has been demonstrated to possibly lead to drifting and localization of reentrant drivers in a human atrial model.

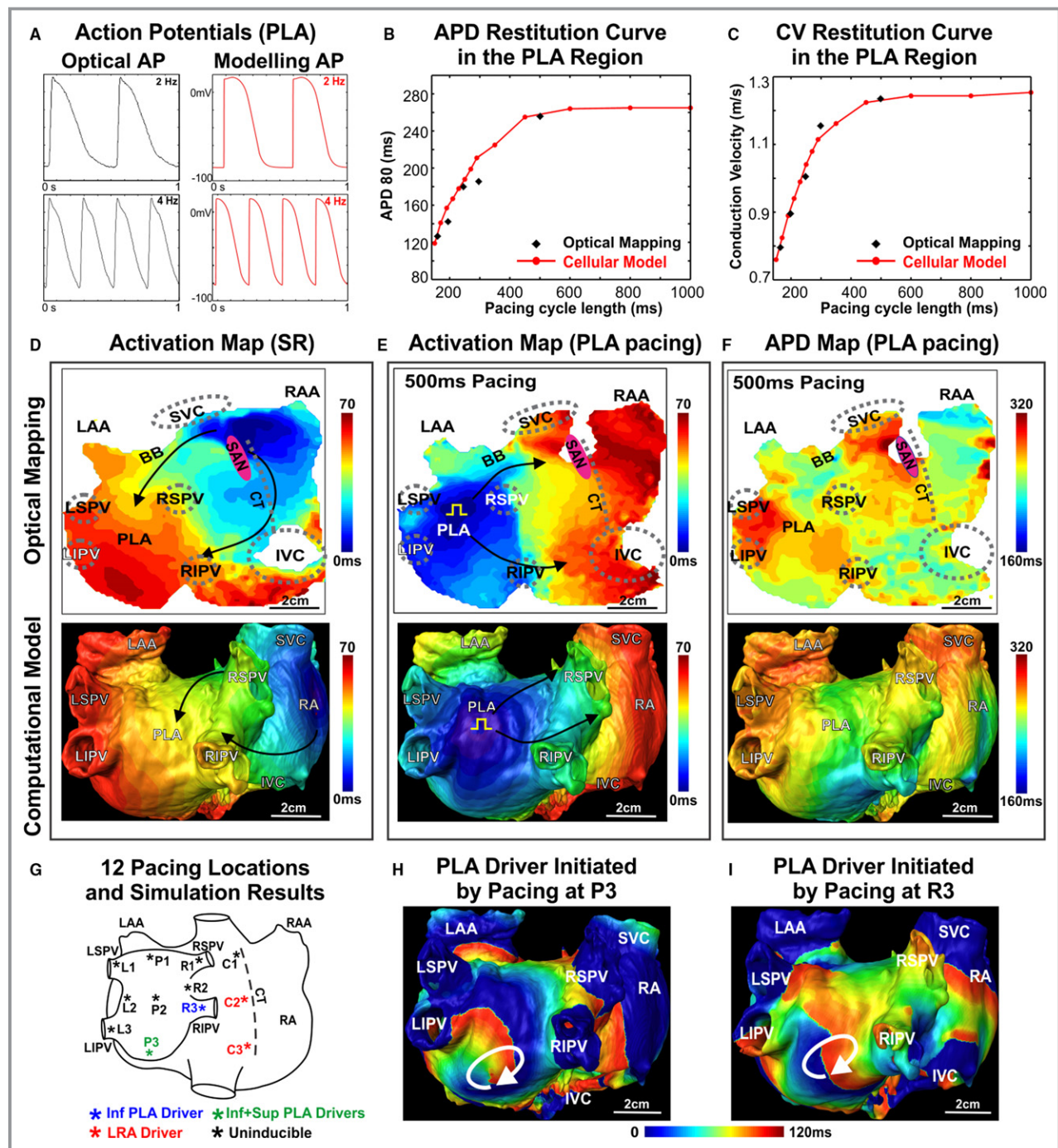


Figure 8. The 3-dimensional computer models were developed to reproduce the electrical propagation patterns consistent with optical mapping data and test AF inducibility and maintenance. A, PLA action potentials (APs) during 2- and 4-Hz pacing for the adapted Fenton-Karma cellular model (left) and optically recorded APs (right). Action potential duration (APD) restitution curve (B) and conduction velocity (CV) restitution curve (C) for the adapted Fenton-Karma cellular model during PLA pacing based on optical mapping data. Optical mapping (top) and the computational model (bottom) map electrical activation patterns (curved arrows) during sinus rhythm (SR) (D) and during PLA pacing (E) and visualize APD distribution during PLA pacing (F). G, Twelve locations across the atria selected as pacing sites for computer simulations. The pacing locations at which AF was induced or block occurred are shown as colored stars on the atrial image. Computer simulation reproduced the inferior PLA reentrant AF driver when paced from the atrial floor (H) and from the RIPV (I). AF indicates atrial fibrillation; BB, Bachmann’s bundle; CT, crista terminalis; Inf, inferior; IVC/SVC, inferior/superior vena cava; RA, right atrium; LAA/RAA, left/right atrial appendage; LRA, lateral right atrium; LSPV/LIPV/RSPV/RIPV, left superior/left inferior/right superior/right inferior pulmonary vein; PLA, posterior left atrium; SAN, sino-atrial node; Sup, superior.

Table. 3-Dimensional Atrial Structural Measurements of the Explanted Human Atria From the Contrast-Enhanced MRI Data Analysis

Atrial Tissue and Cavity Volume							
		Left Atrium		Right Atrium		Whole Atria*	
Tissue volume		30.7 cm ³		37.2 cm ³		74.2 cm ³	
Cavity volume		41.4 cm ³		47.4 cm ³		88.8 cm ³	
Wall Thickness							
		Left Atrium		Right Atrium		Whole Atria	
Max		8.60 mm		11.7 mm		11.7 mm	
Upper quartile		4.5 mm		5.6 mm		5.0 mm	
Median		3.4 mm		3.8 mm		3.6 mm	
Lower quartile		2.5 mm		2.5 mm		2.5 mm	
Minimum		1.1 mm		0.4 mm		0.4 mm	
Mean		3.7 mm		4.2 mm		4.0 mm	
SD		1.7 mm		2.3 mm		2.0 mm	
Fibrosis							
Left Atrium				Right Atrium			
Overall Fibrosis %		23.2%		Overall Fibrosis %		12.4%	
2 Transmural Partitions		3 Transmural Partitions		2 Transmural Partitions		3 Transmural Partitions	
Sub-Epi	7.5%	Sub-Epi	4.2%	Sub-Epi	4.0%	Sub-Epi	2.6%
Sub-Endo	48.5%	Midwall	21.6%	Sub-Endo	21.2%	Midwall	9.5%
		Sub-Endo	61.9%			Sub-Endo	25.7%
Whole Atria* (16.6%)							
2 Transmural Partitions				3 Transmural Partitions			
Sub-Epi	5.5%			Sub-Epi	3.4%		
Sub-Endo	30.3%			Midwall	14.2%		
				Sub-Endo	36.9%		

Epi, epicardium; Endo, endocardium; MRI, magnetic resonance imaging. *Includes left atrium, right atrium, and interatrial septum.

Moreover, development and progression of atrial fibrosis is widely accepted as one of the most important substrates for AF perpetuation by inducing marked local conduction abnormalities.^{4,5} Recent clinical studies in AF patients using in vivo late gadolinium-enhanced MRI suggest that the extent and distribution of atrial fibrosis is a reliable predictor of catheter ablation success.^{6,9} Our recent studies of human RA ex vivo using high-resolution CE-MRI directly demonstrated that the combination of increased intramural fibrotic strands, greater endo-epicardial myofiber misalignment, and atrial thickness variation may create microanatomic tracks for stable reentrant AF drivers.^{7,8}

Existing Structural Analysis Methodologies

Early knowledge on atrial fiber orientations has been obtained by Ho and colleagues using photography and tracings of

visually observed myofiber tracts after manually dissecting human hearts.³⁰ The first complete quantitative description of whole intact sheep atria myofiber architecture was done using serial surface imaging and 3D structure tensor analysis.^{15,27} The structure tensor approach was extended to explanted human atria imaged by our recent studies using CE-MRI,⁸ and micro-computed tomography¹⁹ proved to be as robust an approach as diffusion tensor imaging.²⁰ In the past, numerous wall thickness estimation approaches have been developed for cardiac chambers.²⁵ The most straightforward approaches, such as the nearest neighbor method, which calculates the shortest distance between the epicardial and endocardial surfaces, or the normal-based method, which calculates the length of lines normal to the epicardial surface within a region, are error prone.^{8,25,26} A robust approach for 3D atrial wall thickness estimation across the atrial chambers is to solve the Laplace equation.²⁵ Furthermore, fibrosis was

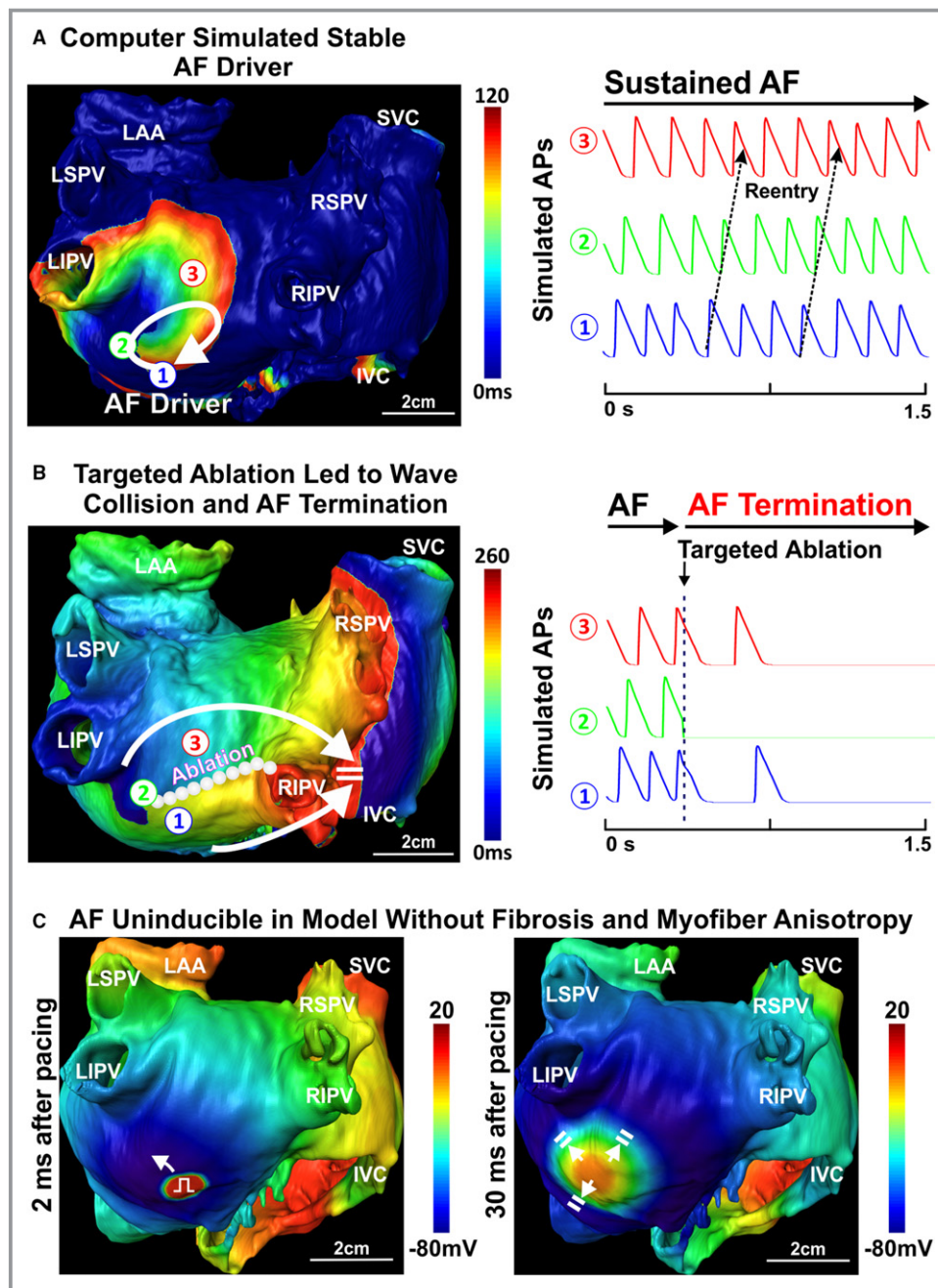


Figure 9. Realistic 3-dimensional (3D) human atrial computer models can test ablation strategies for AF termination as well as the role structure plays in AF induction. A, The PLA reentrant driver was replicated by burst pacing from the atrial floor with computer simulation. Action potentials (APs) from locations 1 to 3 are displayed. B, The ablation strategy that created a linear transmural ablation lesion from the reentrant pivoting point to the nearby physical border effectively terminated AF. C, Using the same pacing protocol and location from the atrial floor that previously induced sustained AF, but with fibrosis and 3D myofiber data removed from the model, led to conduction failure. AF indicates atrial fibrillation; IVC/SVC, inferior/superior vena cava; LAA, left atrial appendage; LSPV/LIPV/RSPV/RIPV, left superior/left inferior/right superior/right inferior pulmonary vein; PLA, posterior left atrium.

typically identified by thresholding techniques, such as SDs above a reference by us^{23,24} and others,⁴² a blood-pool-based reference,⁴³ and adapted histogram algorithm.²² The

Trayanova group²² was the first to devise a novel structural analysis to quantitate fibrosis patterns across the human atria using fibrosis density and entropy, and linked these

parameters to AF driver locations. To date, there is no single study that has integrated all 3 structural components that may compose AF driver fingerprints.^{4,7,8}

An Integrated Approach to Resolve Human AF Driver Structural Fingerprints

Computer models provide a powerful tool for quantitative examination of structural substrates and their individual contribution to AF mechanisms.^{6,11} Our results from computer models in the presence or absence of structure suggested that atrial structure itself may be necessary for reentry initiation and maintenance. The recent computer simulation work by Gonzales et al examined the impact of atrial structural (myofibers and fibrosis) properties on rotor evolution.²⁸ The more recent computer simulation study by the Trayanova group²² based on *in vivo* late gadolinium-enhanced MRI went further and suggested that AF reentrant drivers are perpetuated by fibrosis boundary zones characterized by their fibrotic density and entropy metrics, which are consistent with our findings.

Our study takes the next step in defining AF structural substrates by integrating high-resolution functional data with a 3D structural detailed analysis of atrial wall thickness, fibrosis distribution, and myofiber architecture of entire human atria. In this study, we have further refined fibrosis identification in CE-MRI images via histological staining of the same heart,²⁴ and extended the fiber orientation analysis to the whole human atria imaged using CE-MRI. We also developed a novel computational framework to estimate 3D wall thickness across both atrial chambers.²⁵ We discovered that the 2 localized reentrant AF driver regions functionally identified by optical mapping¹⁹ correlate with certain structural characteristics, such as intermediate regions of atrial wall thickness and fibrosis in regions with twisted transmural myofiber orientations. Furthermore, we have demonstrated that a higher proportion of combined intermediate wall thickness and fibrosis distinguished the 3 atrial drivers (14.4% and 6.7% in inferior and superior PLA, respectively, and 6.4% in LRA) from the rest of the atrial tissue (median 0.03%). Further development of our quantitative analysis may provide an alternative novel approach to the fibrosis density and entropy measurements²² for predicting AF driver regions based on atrial structural fingerprints through noninvasive CE-MRI.

AF Ablation Strategies and Future Directions

Recent clinical studies utilizing different ablation strategies (eg, PV isolation and FIRM, Focal Impulse and Rotor Modulation) yielded varying results/outcomes.^{3,6,35,44} Importantly, ablation lesion sets are not reversible, so the success of different procedures can never be compared for the same

patient.^{13,45} The computer modeling approach is currently the only way to compare a variety of ablation strategies on the same heart and can be used for ablation planning and guidance.^{14,36} Earlier computer modeling studies were utilized to test the effectiveness of different PV isolation ablation patterns^{45–47} and to evaluate ablation lesion gaps.^{11,48} A recent study identified optimal ablation targets with smallest amount of tissue ablated to terminate left atrial flutter using patient-specific models based on *in vivo* late gadolinium-enhanced MRI.⁴³

Since our method showed that the human atrial wall could vary in thickness from 0.4 to 11.7 mm, the detailed knowledge of atrial wall thickness variation could help plan the power and timing of any ablation procedure to ensure transmural lesions with no collateral damage to structures outside the heart.²⁵ Furthermore, if AF drivers are identified, our proposed single-line ablation approach required $\approx 50\%$ less tissue destruction for successful termination of AF compared with other driver-targeting ablation strategies (Figure 9 and Figure S3B). We plan to conduct a systematic structural analysis for a large number of *ex vivo* human atria mapped with integrated high-resolution CE-MRI and optical mapping using the computational framework outlined here to define structural fingerprints universal among reentrant AF drivers and design optimal ablation procedures.

Study Limitations

Our study is limited, as it is based on 1 explanted diseased human heart, and all our observations are specific for this heart. Future studies are necessary to apply the novel 3D computational high-resolution framework in a greater amount of human hearts with a variety of disease history to define reproducible AF driver fingerprints. There were 3 optically identified AF driver regions in this human heart and only the inferior PLA and LRA drivers were used for initial quantitative analysis characterizing fingerprints, since the precise location of the superior PLA driver track was not seen well by optical mapping. The fixation process of the atria may affect size and thickness variation measurements derived from *ex vivo* CE-MRI by $\approx 5\%$ as shown by other studies.⁴⁹ The computed atrial wall thickness in the left atrial appendage was found to be affected by the extremely complex and trabecular atrial anatomy,³⁰ and thus wall thickness of the left atrial appendage was not reported. The atrial cellular activation model is based on a simplified Fenton-Karma model, not biophysics-based cellular models^{10,12} for the sake of computational efficiency, although it was validated by optical mapping data in this study and widely used by us^{15,27} and others.²⁸ Additionally, because of a single uniform cellular model used across the atria in the computer model, APDs in some regions (eg, distal side of PV sleeves) may not match

well between modeling and optical mapping. Nevertheless, APD values across the RA (209–320 ms) and LA (210–312 ms) for both optical mapping and the computer simulation are within the range of clinical monophasic action potential measurements of RA (209–351 ms) and LA (202–339 ms) in patients with and without AF history.^{50,51} A family of cellular models will need to be developed and used in the 3D computer model to match entire atrial regional cellular heterogeneity. Finally, the ex vivo human heart was denervated and without the external influence of the autonomic nervous system and metabolic stresses that are known to play a critical role in AF.³⁹ However, explanted human hearts give us the unique opportunity to control autonomic influence and evaluate AF mechanisms at different levels of autonomic stimulation. In our study, all presented functional data were recorded during isoproterenol, which is commonly used in clinical studies of AF,^{44,52–54} to recapitulate the influence of autonomic stimulation.

Conclusions

Our novel integrative approach combining ex vivo functional and 3D structural imaging at the highest resolution to date, with computer simulation of intact human atria provides for the first time detailed 3D analysis of wall thickness, myofiber orientation, and transmural fibrosis to define the heart-specific structural fingerprints of AF drivers. The further development of 3D computational models based on ex vivo human heart studies may allow defining fingerprints of AF drivers that can be applied to AF driver identification in vivo.

Acknowledgments

We sincerely thank the Lifeline of Ohio Organ Procurement Organization and the Division of Cardiac Surgery at The OSU Wexner Medical Center for providing the explanted hearts. We would like to thank Dr Stanislav Zakharkin for his assistance in statistical analysis.

Sources of Funding

This work was supported by NIH HL115580 and HL135109 (Fedorov), HL113084 (Janssen), HL084583, HL083422, HL114383 (Mohler), by funding from Dorothy M. Davis Heart and Lung Research Institute, and American Heart Association Grant in Aid #16GRNT31010036 (Fedorov), and by the Health Research Council of New Zealand and National Heart Foundation of New Zealand (Zhao).

Disclosures

None.

References

- Gillis AM, Krahn AD, Skanes AC, Nattel S. Management of atrial fibrillation in the year 2033: new concepts, tools, and applications leading to personalized medicine. *Can J Cardiol*. 2013;10:114–1146.
- Tilz RR, Rillig A, Thum AM, Arya A, Wohlmuth P, Metzner A, Mathew S, Yoshiga Y, Wissner E, Kuck KH, Ouyang F. Catheter ablation of long-standing persistent atrial fibrillation: 5-year outcomes of the Hamburg Sequential Ablation Strategy. *J Am Coll Cardiol*. 2012;60:1921–1929.
- Woods CE, Olgin J. Atrial fibrillation therapy now and in the future: drugs, biologicals, and ablation. *Circ Res*. 2014;114:1532–1546.
- Small BH, Zhao J, Trew ML. Three-dimensional impulse propagation in myocardium arrhythmogenic mechanisms at the tissue level. *Circ Res*. 2013;112:834–848.
- Trayanova NA. Mathematical approaches to understanding and imaging atrial fibrillation significance for mechanisms and management. *Circ Res*. 2014;114:1516–1531.
- Haissaguerre M, Shah AJ, Cochet H, Hocini M, Dubois R, Efimov I, Vigmond E, Bernus O, Trayanova N. Intermittent drivers anchoring to structural heterogeneities as a major pathophysiological mechanism of human persistent atrial fibrillation. *J Physiol*. 2016;594:2387–2398.
- Hansen BJ, Csepe TA, Zhao J, Ignozzi AJ, Hummel JD, Fedorov VV. Maintenance of atrial fibrillation: are reentrant drivers with spatial stability the key? *Circ Arrhythm Electrophysiol*. 2016;9:e004398.
- Hansen BJ, Zhao J, Csepe TA, Moore BT, Li N, Jaynem LA, Kalyanasundaram A, Lim P, Bratasz A, Powell KA, Simonetti OP, Higgins RSD, Kilic A, Mohler PJ, Janssen PML, Weiss R, Hummel JD, Fedorov VV. Atrial fibrillation driven by micro-anatomic intramural re-entry revealed by simultaneous sub-epicardial and sub-endocardial optical mapping in explanted human hearts. *Eur Heart J*. 2015;36:2390–2401.
- Akoum N, Wilber D, Hindricks G, Jais P, Cates J, Marchlinski F, Kholmovski E, Burgon N, Hu N, Mont L, Deneke T, Duytschaever M, Neumann T, Mansour M, Mahnkopf C, Hutchinson M, Herweg B, Daoud E, Wissner E, Brachmann J, Marrouche NF. MRI assessment of ablation-induced scarring in atrial fibrillation: analysis from the DECAAF Study. *J Cardiovasc Electrophysiol*. 2015;26:473–480.
- Seemann G, Höper C, Sachse FB, Dössel O, Holden AV, Zhang H. Heterogeneous three-dimensional anatomical and electrophysiological model of human atria. *Philos Trans A Math Phys Eng Sci*. 2006;364:1465–1481.
- Dössel O, Krueger MW, Weber FM, Wilhelms M, Seemann G. Computational modeling of the human atrial anatomy and electrophysiology. *Med Biol Eng Comput*. 2012;50:773–799.
- Colman MA, Castro SJ, Alday EAP, Hancox JC, Garratt C, Zhang H. Recent progress in multi-scale models of the human atria. *Drug Discov Today Dis Models*. 2014;14:23–32.
- Zhao J, Kharche SR, Hansen BJ, Csepe TA, Wang E, Stiles MK, Fedorov VV. Optimization of catheter ablation of atrial fibrillation: insights gained from clinically-derived computer models. *Int J Mol Sci*. 2015;16:10834–10854.
- Haissaguerre M, Lim K-T, Jacquemet V, Rotter M, Dang L, Hocini M, Matsuo S, Knecht S, Jais P, Virag N. Atrial fibrillatory cycle length: computer simulation and potential clinical importance. *Europace*. 2007;9:vi64–vi70.
- Zhao J, Butters TD, Zhang H, Pullan AJ, LeGrice IJ, Sands GB, Small BH. An image-based model of atrial muscular architecture: effects of structural anisotropy on electrical activation. *Circ Arrhythm Electrophysiol*. 2012;5:361–370.
- Klos M, Calvo D, Yamazaki M, Zlochiver S, Mironov S, Cabrera J-A, Sanchez-Quintana D, Jalife J, Berenfeld O, Kalifa J. Atrial septopulmonary bundle of the posterior left atrium provides a substrate for atrial fibrillation initiation in a model of vagally mediated pulmonary vein tachycardia of the structurally normal heart. *Circ Arrhythm Electrophysiol*. 2008;1:175–183.
- Verheule S, Tuyls E, Gharaviri A, Hulsmans S, van Hunnik A, Kuiper M, Serroyen J, Zeemering S, Kuijpers NH, Schotten U. Loss of continuity in the thin epicardial layer because of endomyocardial fibrosis increases the complexity of atrial fibrillatory conduction. *Circ Arrhythm Electrophysiol*. 2013;6:202–211.
- Verheule S, Eckstein J, Linz D, Maesen B, Bidar E, Gharaviri A, Schotten U. Role of endo-epicardial dissociation of electrical activity and transmural conduction in the development of persistent atrial fibrillation. *Prog Biophys Mol Biol*. 2014;115:173–185.
- Zhao J, Hansen BJ, Csepe TA, Lim P, Wang E, Williams M, Mohler P, Janssen PML, Weiss R, Hummel JD, Fedorov VV. Integration of high resolution optical mapping and 3D micro-CT imaging to resolve the structural basis of atrial conduction in the human heart. *Circ Arrhythm Electrophysiol*. 2015;8:1514–1517.
- Pashakhanloo F, Herzka DA, Ashikaga H, Mori S, Gai N, Bluemke DA, Trayanova NA, McVeigh ER. Myofiber architecture of the human atria as revealed by submillimeter diffusion tensor imaging. *Circ Arrhythm Electrophysiol*. 2016;9:e004133.

21. McDowell KS, Zahid S, Vadakkumpadan F, Blauer J, MacLeod RS, Trayanova NA. Virtual electrophysiological study of atrial fibrillation in fibrotic remodeling. *PLoS One*. 2015;10:e0117110.
22. Zahid S, Cochet H, Boyle PM, Schwarz EL, Whyte KN, Vigmond EJ, Dubois R, Hocini M, Haïssaguerre M, Jais P. Patient-derived models link re-entrant driver localization in atrial fibrillation to fibrosis spatial pattern. *Cardiovasc Res*. 2016;110:443–454.
23. Csepe TA, Zhao J, Sul LV, Wang Y, Hansen BJ, Li N, Ignozzi AJ, Bratasz A, Powell KA, Kilic A, Mohler P, Janssen PML, Hummel JD, Simonetti OP, Fedorov VV. Novel application of 3D contrast-enhanced CMR to define fibrotic structure of the human sinoatrial node in vivo. *Eur Heart J Cardiovasc Imaging*. 2017;18:862–869.
24. Csepe TA, Zhao J, Hansen BJ, Li N, Sul LV, Lim P, Wang E, Simonetti OP, Kilic A, Mohler P, Janssen PML, Fedorov VV. Human sinoatrial node structure: 3D microanatomy of sinoatrial conduction pathways. *Prog Biophys Mol Biol*. 2016;120:164–178.
25. Bishop M, Rajani R, Plank G, Gaddum N, Carr-White G, Wright M, O'Neill M, Niederer S. Three-dimensional atrial wall thickness maps to inform catheter ablation procedures for atrial fibrillation. *Europace*. 2016;18:376–383.
26. Varela M, Kolbitsch C, Theron A, Morgan R, Henningsson M, Schaeffter T, Aslanidi O. 3D high-resolution atrial wall thickness maps using black-blood PSIR. *J Cardiovasc Magn Reson*. 2015;17:P239.
27. Zhao J, Butters TD, Zhang H, LeGrice IJ, Sands GB, Smail BH. Image-based model of atrial anatomy and electrical activation: a computational platform for investigating atrial arrhythmia. *IEEE Trans Med Imaging*. 2013;32:18–27.
28. Gonzales MJ, Vincent KP, Rappel W-J, Narayan S, McCulloch AD. Structural contributions to fibrillatory rotors in a patient-derived computational model of the atria. *Europace*. 2014;16:iv3–iv10.
29. Kazbanov IV, Ten Tusscher KH, Panfilov AV. Effects of heterogeneous diffuse fibrosis on arrhythmia dynamics and mechanism. *Sci Rep*. 2016;6:20835.
30. Ho SY, Cabrera JA, Sánchez-Quintana D. Left atrial anatomy revisited. *Circ Arrhythm Electrophysiol*. 2012;5:220–228.
31. Lewis ST, Drury AN, Iliescu CC. Further observations upon the state of rapid re-excitation of the auricles. *Heart*. 1921;8:311–340.
32. Schuessler RB, Grayson TM, Bromberg BI, Cox JL, Boineau JP. Cholinergically mediated tachyarrhythmias induced by a single extrastimulus in the isolated canine right atrium. *Circ Res*. 1992;71:1254–1267.
33. Cox JL, Canavan T, Schuessler R, Cain M, Lindsay B, Stone C, Smith P, Corr P, Boineau J. The surgical treatment of atrial fibrillation. II. Intraoperative electrophysiologic mapping and description of the electrophysiologic basis of atrial flutter and atrial fibrillation. *J Thorac Cardiovasc Surg*. 1991;101:406–426.
34. Jalife J, Berenfeld O, Mansour M. Mother rotors and fibrillatory conduction: a mechanism of atrial fibrillation. *Cardiovasc Res*. 2002;54:204–216.
35. Narayan SM, Zaman JAB. Mechanistically-based mapping of human cardiac fibrillation. *J Physiol*. 2016;594:2399–2415.
36. Haïssaguerre M, Hocini M, Denis A, Shah AJ, Komatsu Y, Yamashita S, Daly M, Amraoui S, Zellerhoff S, Picat M-Q. Driver domains in persistent atrial fibrillation. *Circulation*. 2014;130:530–538.
37. Alessie MA, de Groot NM, Houben RP, Schotten U, Boersma E, Smeets JL, Crijns HJ. Electropathological substrate of long-standing persistent atrial fibrillation in patients with structural heart disease longitudinal dissociation. *Circ Arrhythm Electrophysiol*. 2010;3:606–615.
38. Lee G, Kumar S, Teh A, Madry A, Spence S, Larobina M, Goldblatt J, Brown R, Atkinson V, Moten S. Epicardial wave mapping in human long-lasting persistent atrial fibrillation: transient rotational circuits, complex wavefronts, and disorganized activity. *Eur Heart J*. 2014;35:86–97.
39. Csepe TA, Hansen BJ, Fedorov VV. Atrial fibrillation driver mechanisms: insight from the isolated human heart. *Trends Cardiovasc Med*. 2017;27:1–11.
40. Spach MS, Miller W, Dolber PC, Kootsey JM, Sommer JR, Mosher C. The functional role of structural complexities in the propagation of depolarization in the atrium of the dog. Cardiac conduction disturbances due to discontinuities of effective axial resistivity. *Circ Res*. 1982;50:175–191.
41. Spach M, Dolber P, Heidlage J. Influence of the passive anisotropic properties on directional differences in propagation following modification of the sodium conductance in human atrial muscle. A model of reentry based on anisotropic discontinuous propagation. *Circ Res*. 1988;62:811–832.
42. Pontecorboli G, Ventura RMF, Carlosena A, Benito E, Prat-Gonzales S, Padeletti L, Mont L. Use of delayed-enhancement magnetic resonance imaging for fibrosis detection in the atria: a review. *Europace*. 2017;19:180–189.
43. Chrispin J, Ipek EG, Zahid S, Prakosa A, Habibi M, Spragg D, Marine JE, Ashikaga H, Rickard J, Trayanova NA. Lack of regional association between atrial late gadolinium enhancement on cardiac magnetic resonance and atrial fibrillation rotors. *Heart Rhythm*. 2016;13:654–660.
44. Benharash P, Buch E, Frank P, Share M, Tung R, Shivkumar K, Mandapati R. Quantitative analysis of localized sources identified by focal impulse and rotor modulation mapping in atrial fibrillation. *Circ Arrhythm Electrophysiol*. 2015;8:554–561.
45. Jacquemet V. Lessons from computer simulations of ablation of atrial fibrillation. *J Physiol*. 2016;594:2417–2430.
46. Virag N, Jacquemet V, Kappenberger L. Modeling of atrial fibrillation. In: *Cardiac Mapping*. 4th ed. Shenasa M, Hindricks G, Borggrefe M, Breithardt G, Josephson ME, Wiley-Blackwell: Oxford, UK; 2012:131–139.
47. Dang L, Virag N, Ihara Z, Jacquemet V, Vesin J-M, Schlaepfer J, Ruchat P, Kappenberger L. Evaluation of ablation patterns using a biophysical model of atrial fibrillation. *Ann Biomed Eng*. 2005;33:465–474.
48. Krueger MW, Schulze WH, Rhode KS, Razavi R, Seemann G, Dössel O. Towards personalized clinical in-silico modeling of atrial anatomy and electrophysiology. *Med Biol Eng Compu*. 2013;51:1251–1260.
49. Tran T, Sundaram CP, Bahler CD, Eble JN, Grignon DJ, Monn MF, Simper NB, Cheng L. Correcting the shrinkage effects of formalin fixation and tissue processing for renal tumors: toward standardization of pathological reporting of tumor size. *J Cancer*. 2015;6:759–766.
50. Nakai T, Watanabe I, Kunimoto S, Kojima T, Kondo K, Saito S, Ozawa Y, Kanmatsuse K. Electrophysiological effect of adenosine triphosphate and adenosine on atrial and ventricular action potential duration in humans. *Jpn Circ J*. 2000;64:430–435.
51. Narayan SM, Kazi D, Krummen DE, Rappel W-J. Repolarization and activation restitution near human pulmonary veins and atrial fibrillation initiation: a mechanism for the initiation of atrial fibrillation by premature beats. *J Am Coll Cardiol*. 2008;52:1222–1230.
52. Miller JM, Kowal RC, Swarup V, Daubert JP, Daoud EG, Day JD, Ellenbogen KA, Hummel JD, Baykaner T, Krummen DE. Initial independent outcomes from focal impulse and rotor modulation ablation for atrial fibrillation: multicenter FIRM registry. *J Cardiovasc Electrophysiol*. 2014;25:921–929.
53. Kurotobi T, Shimada Y, Kino N, Ito K, Tomomura D, Yano K, Tanaka C, Yoshida M, Tsuchida T, Fukumoto H. Residual arrhythmogenic foci predict recurrence in long-standing persistent atrial fibrillation patients after sinus rhythm restoration ablation. *Can J Cardiol*. 2014;30:1535–1540.
54. Oral H, Crawford T, Frederick M, Gadeela N, Wimmer A, Dey S, Sarrazin JF, Kuhne M, Chalfoun N, Wells D. Inducibility of paroxysmal atrial fibrillation by isoproterenol and its relation to the mode of onset of atrial fibrillation. *J Cardiovasc Electrophysiol*. 2008;19:466–470.

SUPPLEMENTAL MATERIAL

Data S1.

Supplemental Methods

Ex-vivo MRI of human atria

Contrast-enhanced MRI (CE-MRI) was used to define surface geometry and micro-structure of atria as previously described.¹ After the optical mapping experiment, the whole human atria were formalin fixed for 48-72 hours, then washed out with PBS and incubated at 4°C in 0.2% Gd-DTPA (dimeglumine gadopentetate Magnevist, Bayer Schering Pharma) for 7 days in order to perform a CE-MRI. The human atria were imaged at The Ohio State University using a 9.4 T Bruker BioSpin Spectrometer (Ettlingen, Germany) and a 72 mm volume coil. FLASH_3Dslab_bas protocol was used to obtain high-resolution images with the following parameters: echo time 3.4ms, repetition time 16.7ms, flip angle 30°, naver=8 and fat suppression on (BW = 1520 HZ). Volume images with $\sim 180 \times 180 \times 360 \mu\text{m}^3$ resolution and dimensions of $107 \times 61 \times 85 \text{ mm}^3$ were obtained within 5 hours.

A MatLab built-in *Interpolate* function (MathWorks, Inc.) was used to interpolate raw tissue MRI images along the Z-axis to obtain an isotropic resolution of $\sim 180 \mu\text{m}^3$ for this 3D volume. 2D MRI images of the human atria with a resolution of $\sim 180 \mu\text{m}^2$ were segmented using a carefully selected global threshold (134) to effectively eliminate most of the background noise. The whole procedure was processed and visualized in 3D using commercial software Amira (FEI Company). A manual interactive segmentation approach was employed on each 2D imaging slice by visualizing the image data in orthogonal views to help further segment atrial anatomical regions (**Figure 1**), such as pulmonary veins, superior vena cava, coronary sinus, and coronary arteries, and to remove tissue structures that were not directly related to atria (background noise, fat, ventricular tissue etc.). A minimal bounding box was employed on the original CE-MRI images to minimize space and memory usage. Finally a suite of image processing tools were employed to process the high-resolution images to smooth internal structures, extract tissue boundaries, and digitally construct a voxel-based 3D volume (**Figure 1**).² The optical mapping and reconstructed 3D human atrial structure were reconciled using atrial anatomical landmarks.³

3D atrial wall thickness estimation

A robust approach for 3D atrial wall thickness estimation across the two atrial chambers is to solve the Laplace equation with two boundary conditions specified at both epicardial and endocardial surfaces.⁴ As previously seen in our study¹ and others⁵, simpler approaches, such as measuring normal projection or closest point from one surface to the other one, are error-prone.

We have extended this Laplace approach to the whole human atria imaged by CE-MRI. First of all, we needed to close atrial chambers manually by adding artificial barriers to the four pulmonary veins (PVs), mitral valve, tricuspid valve, superior vena cava and inferior vena cava. A region grow function was used to obtain the endocardial surfaces and then the epicardial surface, seeding from the corresponding cavity and background spaces, respectively (Figure S1). The non-surface tissue region and both atrial cavities were also extracted (Figure S2). Finally, 3D atrial wall variation across the two atrial chambers was estimated by solving the Laplace equation and then tracing the trajectories along the gradient field of the Laplace solutions connecting the two surfaces. Atrial cavity/tissue volume, right atrium (RA) vs left atrium (LA), was estimated as well (Table 1).

The Laplace equation for the given 3D human atrial volume is shown below:

$$\frac{\partial^2 \phi}{\partial x^2} + \frac{\partial^2 \phi}{\partial y^2} + \frac{\partial^2 \phi}{\partial z^2} = 0, \quad (1)$$

According to the Taylor expansion, a point ϕ_i and its neighbouring points (ϕ_{i-1} and ϕ_{i+1}) were chosen along the x-axis, with a separation distance of h in one dimension, we obtained the following equations:

$$\phi_{i-1} = \phi_i - \frac{\partial \phi}{\partial x} \Big|_i h + \frac{\partial^2 \phi}{\partial x^2} \Big|_i \frac{h^2}{2!} - \frac{\partial^3 \phi}{\partial x^3} \Big|_i \frac{h^3}{3!} + \frac{\partial^4 \phi}{\partial x^4} \Big|_i \frac{h^4}{4!} - \dots, \quad (2)$$

$$\phi_{i+1} = \phi_i + \frac{\partial \phi}{\partial x} \Big|_i h + \frac{\partial^2 \phi}{\partial x^2} \Big|_i \frac{h^2}{2!} + \frac{\partial^3 \phi}{\partial x^3} \Big|_i \frac{h^3}{3!} + \frac{\partial^4 \phi}{\partial x^4} \Big|_i \frac{h^4}{4!} + \dots, \quad (3)$$

Adding Equations (2) and (3) and removing third and higher order terms, we could rearrange it into the following so-called central difference method⁶:

$$\frac{\partial^2 \phi}{\partial x^2} \Big|_i = \frac{\phi_{i+1} - 2\phi_i + \phi_{i-1}}{h^2}, \quad (4)$$

Extending this into three dimensions, we now had expressions of each of the terms in the 3D Laplace equation. Substituting into Equation (1):

$$\frac{\phi_{i+1} - 2\phi_i + \phi_{i-1}}{h^2} + \frac{\phi_{j+1} - 2\phi_j + \phi_{j-1}}{h^2} + \frac{\phi_{k+1} - 2\phi_k + \phi_{k-1}}{h^2} = 0, \quad (5)$$

Rearranging it into

$$\phi_{i,j,k} = \frac{(\phi_{i+1,j,k} + \phi_{i-1,j,k} + \phi_{i,j+1,k} + \phi_{i,j-1,k} + \phi_{i,j,k+1} + \phi_{i,j,k-1})}{6}, \quad (6)$$

With the above central difference formula, we could solve the Laplace solution with a second-order accuracy iteratively. For each iteration, the maximum relative change for each pixel was calculated in order to decide whether the numerical solution had converged or not:

$$\epsilon(i, j, k) = \left| \frac{\phi^{iteration-1}(i, j, k) - \phi^{iteration}(i, j, k)}{\phi^{iteration-1}(i, j, k)} \right|, \quad (7)$$

In our implementation, the Laplace solver was terminated when numerical solutions were solved with a maximum relative error of 0.02%. Additionally, a successive over relaxation was used to significantly decrease computation time and the most common value for the relaxation factor ($\omega = 1.4$)⁷ was adopted

$$\phi(i, j, k)^{(New)} = (1 - \omega) \phi(i, j, k)^{(Old)} + \omega \phi(\widetilde{l, j, k}), \quad (8)$$

Where $\phi(\widetilde{l, j, k})$ is given by Equation (6).

To solve the Laplace equation (1) or (6) over the 3D atrial volume, constant boundary conditions have to be specified at the epicardial and endocardial surfaces.⁴ In our case, we used 100 and 300 respectively in our 3D numerical solver. Due to the fact that human atria are composed of dual chambers, it was necessary to divide the atrial tissue into RA and LA, and then solve the Laplace equation separately on each atrial chamber.

After obtaining the Laplace solution field, the gradient map was calculated for each of the solutions using MatLab's built-in *gradient* function and then normalised by magnitude at each

point. The 3D wall thickness at any location in atrial volume was estimated by using the following procedures: Starting from any point and its gradient from one surface, a line travelling along the local gradient will keep propagating using a new point and its gradient within the 3D volume, till it reaches the other surface of interest in the Laplace solutions. The distance travelled from the original point on the surface along its traveling path was recorded as the atrial wall thickness. This procedure was then repeated for every point on the surface and therefore, to complete the calculation of the atrial wall thickness map. Finally, a MATLAB built-in interpolation function, `interp3`, was used to smooth the wall thickness map and fill in any unassigned values within the 3D atrial volume.

Other important information we can extract from the Laplace solutions was the transmural of atrial volume. Given that the values of the Laplace solutions varied from 100 (fixed at the epicardium) to 300 (fixed at the endocardium), we chose the regions with values from 175 to 225 as transmural/mid-wall tissue, values smaller than 175 as the subepicardial regions and values larger than 225 as the subendocardial regions. In this way, we can separate the 3D atrial wall into three different partitions and study the difference in atrial structure in these partitions throughout our study.

3D fibrosis distribution estimation

Fibrosis has higher intensity compared with non-fibrotic tissue when imaged using the CE-MRI approach.^{1, 8} Fibrosis percentage was measured from 2D CE-MRI sections by applying a fibrosis enhancement mask. The mask was based on signal intensity threshold differences of connective and muscular tissue, and was validated with 2D histology sections. After the CE-MRI scan, key regions of the same heart were stained by Masson's trichrome with $0.5 \times 0.5 \mu\text{m}^2$ resolution. 3D CE-MRI structures were registered with the corresponding high-resolution histological data using anatomical landmarks, allowing for comparison of similar slice sections in MRI imaging and histology staining (**Figure 3C**). Then, a series of 2D re-sliced CE-MRI images were analyzed to obtain an optimal global threshold value to identify fibrosis throughout the human atria by comparing corresponding histological sections.

To characterize fibrosis in histological data, non-fibrosis pixels must be removed, namely areas dominated by nuclei, cytoplasm (red/purple) and background (white). First, white pixels were filtered out by removing pixels with luminance greater than 128 (uint8 RGB) using a weighted formula ($0.2126 \times \text{red} + 0.7152 \times \text{green} + 0.0722 \times \text{blue}$). Red channel was then filtered out by removing all pixels greater or equal to 100. Next, pixels with insignificant amounts of blue were removed (< 100 in the blue channel). Finally, a median filter was applied to the remaining pixels to capture areas dense in connective tissue, i.e. fibrosis. We also calculated the total tissue area of each histological slice. Then the fibrosis percentage in each 2D section was estimated.

The matched CE-MRI sections were used to find the intensity threshold required to obtain the same fibrosis percentage found from the histological slices for the regions separately. A least square fitting was employed to minimize the difference between the calculated fibrosis percentage in CE-MRI and the expected fibrosis percentage in histological sections. Therefore, a global threshold value (184) for CE-MRI (**Figure 3**) was found.

To evaluate the fibrosis distribution in atrial volume, we color-coded and visualized fibrosis transmurally using a rainbow colour spectrum: blue for endocardium and red for epicardium (**Figure 3**). Furthermore, we measured fibrosis density by counting the percentage of fibrotic voxels out of the total volume of a sphere with a radius of 5 pixels.

Figure S1

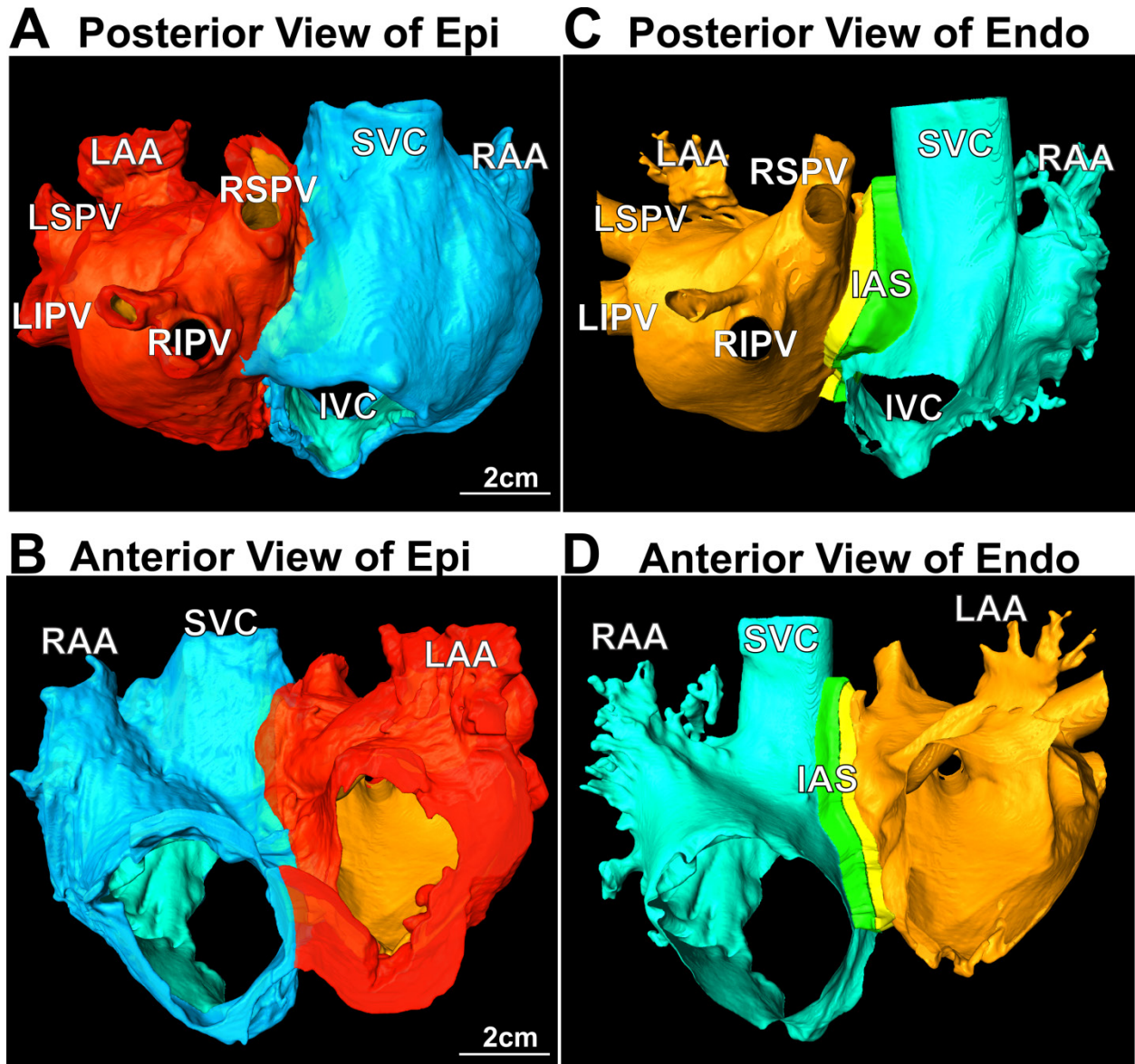


Figure S1. A-D: 3D epi and endo surfaces are shown from posterior and anterior views, respectively. **A** and **B**: the LA and RA epi (red and blue, respectively); **C** and **D**: the LA and RA endo (gold and cyan) and the interatrial septum region (yellow and green). LA/RA – left/right atrium, BB – Bachmann’s bundle, CS – coronary sinus, Endo – endocardium, Epi – epicardium, LS/LI/RS/RI PV – left superior/left inferior/right superior/right inferior pulmonary vein, IAS – interatrial septum, IVC/SVC – inferior/superior vena cava, LAA/RAA – left/right atrial appendage, PLA – posterior left atrium.

Figure S2

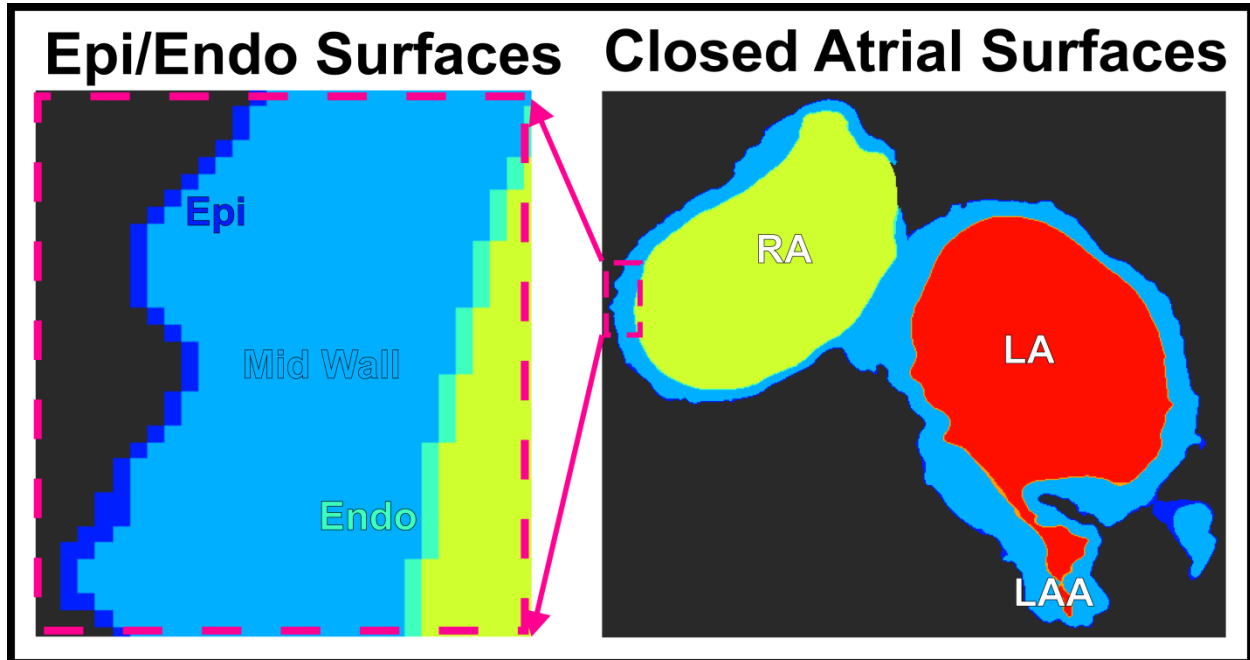
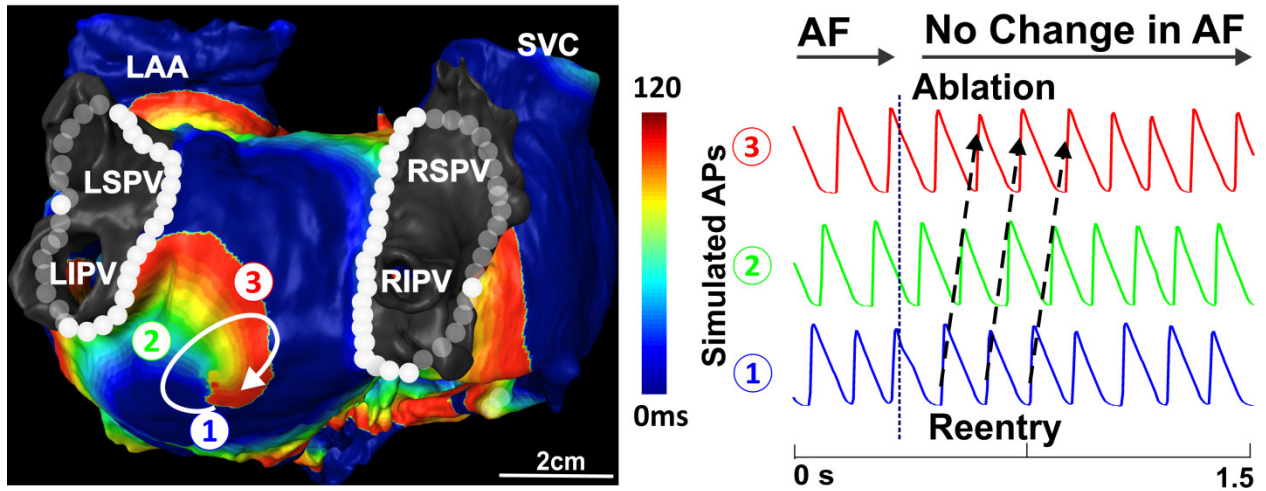


Figure S2. The atrial wall (light blue) of both atrial chambers (LA (red) and RA (green)) were manually closed, and Epi (dark blue) and Endo (teal) surfaces were selected before the Laplace equation was solved for 3D atrial wall thickness. Here a single 2D atrial mask (inferior section of the atria) was displayed, and different regions were highlighted in different colors. LA/RA – left/right atrium, BB – Bachmann’s bundle, CS – coronary sinus, Endo – endocardium, Epi – epicardium, LAA – left atrial appendage.

Figure S3

A PVI Ablation



B Regional Ablation Slows AF

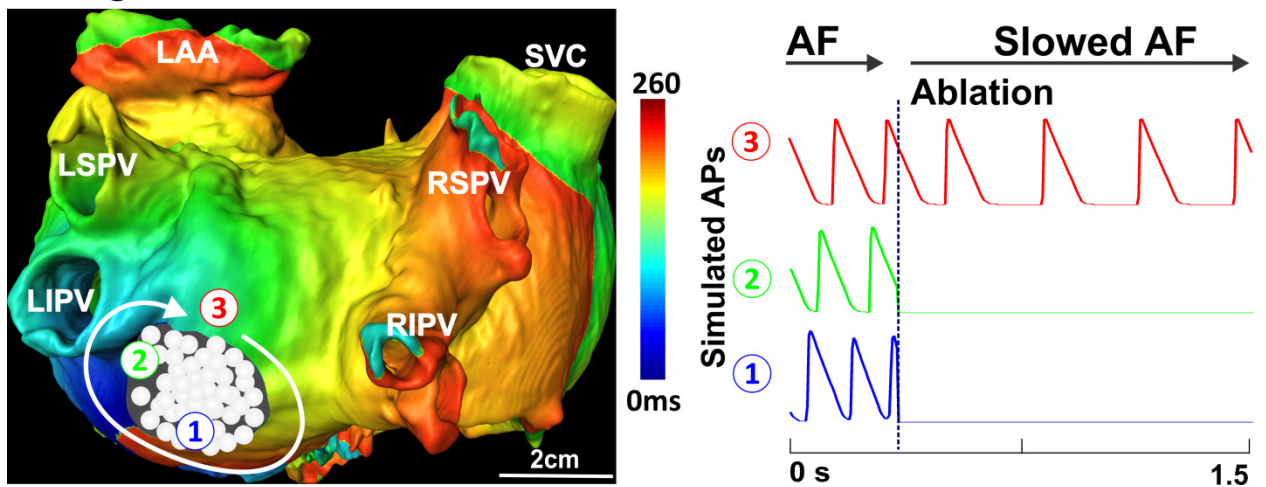


Figure S3. Current clinical ablation strategies failed to terminate atrial fibrillation (AF) in the computer model. **A.** The AF driver at the inferior PLA was replicated in the computer model, and the anatomy-based pulmonary vein isolation (PVI) was employed but had no impact on AF cycle length or maintenance. **B.** A driver regional ablation approach that targeted the area of rotation with an area $\sim 3.1 \text{ cm}^2$ slowed AF. LS/LI/RS/RI PV – left superior/left inferior/right superior/right inferior pulmonary vein, IVC/SVC – inferior/superior vena cava, LAA – left atrial appendage, PLA – posterior left atrium.

Supplemental References:

1. Hansen BJ, Zhao J, Csepe TA, Moore BT, Li N, Jaynem LA, Kalyanasundaram A, Lim P, Bratasz A, Powell KA, Simonetti OP, Higgins RSD, Kilic A, Mohler PJ, Janssen PML, Weiss R, Hummel JD and Fedorov VV. Atrial fibrillation driven by micro-anatomic intramural re-entry revealed by simultaneous sub-epicardial and sub-endocardial optical mapping in explanted human hearts. *European Heart Journal*. 2015;36:2390-401.
2. Csepe TA, Zhao J, Hansen BJ, Li N, Sul LV, Lim P, Wang E, Simonetti OP, Kilic A, Mohler P, Janssen PML and Fedorov VV. Human sinoatrial node structure: 3D microwanatomy of sinoatrial conduction pathways. *Progress in Biophysics and Molecular Biology*. 2016;120:164-178.
3. Zhao J, Hansen BJ, Csepe TA, Lim P, Wang E, Williams M, Mohler P, Janssen PML, Weiss R, Hummel JD and Fedorov VV. Integration of high resolution optical mapping and 3D micro-CT imaging to resolve the structural basis of atrial conduction in the human heart. *Circulation: Arrhythmia and Electrophysiology* 2015;8:1514-17.
4. Bishop M, Rajani R, Plank G, Gaddum N, Carr-White G, Wright M, O'Neill M and Niederer S. Three-dimensional atrial wall thickness maps to inform catheter ablation procedures for atrial fibrillation. *Europace*. 2016;18:376-383.
5. Varela M, Kolbitsch C, Theron A, Morgan R, Henningsson M, Schaeffter T and Aslanidi O. 3D high-resolution atrial wall thickness maps using black-blood PSIR. *Journal of Cardiovascular Magnetic Resonance*. 2015;17:P239.
6. Zhao J and Corless RM. Compact finite difference method for integro-differential equations. *Applied mathematics and computation*. 2006;177:271-288.
7. Zhao J, Davison M and Corless RM. Compact finite difference method for American option pricing. *Journal of Computational and Applied Mathematics*. 2007;206:306-321.
8. Akoum N, Wilber D, Hindricks G, Jais P, Cates J, Marchlinski F, Kholmovski E, Burgon N, Hu N, Mont L, Deneke T, Duytschaever M, Neumann T, Mansour M, Mahnkopf C, Hutchinson M, Herweg B, Daoud E, Wissner E, Brachmann J and Marrouche NF. MRI Assessment of Ablation-Induced Scarring in Atrial Fibrillation: Analysis from the DECAAF Study. *Journal of Cardiovascular Electrophysiology*. 2015;26:473-480.